Chiral Molecules in Intense Laser Fields

Maye Alsaawy

Thesis submitted to the University of Ottawa

in partial fulfillment of the

requirements for the

degree of M.Sc. in Physics

Ottawa-Carleton Institute of Physics

Faculty of Science

Department of Physics

University of Ottawa

0.1 Acknowledgement

I would like to thank my supervisor , Prof. Ravi Bhardwaj for giving me the opportunity to join his Ultrafast Photonics Group. I strongly appreciate his support, guidance and help to complete this thesis. I also want to thank Amit Bagga, my previous colleague in the research group for his support during the beginning of my master's. My thanks are extended to the rest of the group members for providing a good work atmosphere.

Above all, I praise Allah, the almighty, for providing me this opportunity and granting me the capability to proceed successfully. To my parents, Abdullah Alsaawy and Fatimah Almetaq, thank you for their continuous and unparalleled love, help and support. I would like to extend my sincere thanks to my sisters and brothers who are never wavered in their support. Words cannot express how grateful I am to my husband Badr Alharbi for his patience and encouragement during my master's study. Special thanks to my beloved son Haitham for all my happy moments with him. Finally, I cannot begin to express my thanks to my friends (Maraim, Nadarah, Mona and Nawaem) Who never let me down when I needed them.

Contents

List of Figures

0.2 Abstract

Chiral molecules play a prominent role in diverse fields such as biochemistry, physics, biology and most importantly pharmaceutical industry. Chiral molecules are non-superimposable mirror images of each other. Every species in nature shows specific chiral properties in chemical structures as well as macroscopic anatomy. Humans left and right hand are an example of chirality, you cannot superimpose them no matter how you rotate them. The left and right-handed molecules are known as enantiomers. They have the same number of atoms but they are arranged differently. Additionally, chiral molecules have identical physical and chemical properties, yet the two enantiomers interact differently with chiral light or with another chiral molecule. Chiral molecules do not exist equally in nature, some of these molecules exist only in one form of the two enantiomers such as sugars, amino acid, enzymes and DNA. This plays an important role in pharmaceutical industry because different enantiomers of a chiral drug will have different effects on our cells. These enantiomers can often exhibit different metabolism rate, potency, or toxicity. For example, the S-enantiomer citalopram which is used to treat depression is 30 times stronger than the R-enantiomer. Therefore, techniques for detecting and quantifying chirality are very important tools for drug development.

The interaction of light with matter gives us the insight to understand enantiomer structure and the ability to distinguish them. Advances in laser technology have enabled the study of molecular interactions with light, specifically, intense light pulses. Due to the importance of chiral differentiation, several techniques have been developed. However, these techniques have their limitations, for example, the drawback of the circular dichroism method is that the measurement is done in liquid samples and has poor sensitivity. Thus, this led to the

development of the photoelectron technique to avoid solvent effects. Furthermore, in the case of the Coulomb explosion method, it cannot be done with large molecules because it is hard to detect all the fragments. Finally, the high harmonic generation method by Cireasa et al (2015); is complicated and consists of three steps as described in section (1.2.5). Therefore, in this thesis, we used a new simple technique to detect chirality. Molecular photoionization enables chiral discrimination via mass spectrometry depending on elliptical polarized light. This thesis demonstrates the ability of photoionization mass spectrometry to discriminate enantiomers using elliptically polarized light. The first chapter describes existing techniques to characterize chiral molecules and the most used technique to study chirality as well as a description of strong field ionization with the emphasis on the process of photoionization which results in chiral discrimination. The second chapter of this thesis describes the experimental methods and strong field double ionization technique capable of distinguishing chirality. The third chapter contains the results and discussion. The last chapter presents the future work and conclusion.

Chapter 1

Background

1.1 Overview

Chiral molecules are non-superimposable mirror images of each other. Human hands are an example of chirality as the left and right hands are mirror images of each other but can not be superimposed. It is also present in nature both in living organisms (plants, animals) and in spiral galaxies Fig1.1 [1] [2]. Snails, for example, can show handedness, some of them have shells that spiral in the right direction, while others have left-handed shells Fig1.2 [3]. An interesting biological phenomenon that exhibits chiral rotation is the chewing motion of cows [4]. Some cows chew food by moving jaws in a clockwise direction and other in a counter-clockwise direction [4]. Some screws are mirror images of each other and are not superimposable. They can have right or left handed threads, therefore they are chiral. The first application of chiro-dynamics is Archimedes screw which was used to transfer water to

the top of a large ship Fig1.3. It is a hollow pipe with a chiral screw inside of it. Archimedes showed that a combination of rotation and chiral structure induce a translation. The screw was operated and turned by manual labour or motor. By rotating the screw, the water is pushed up and comes out from the pipe at the top.

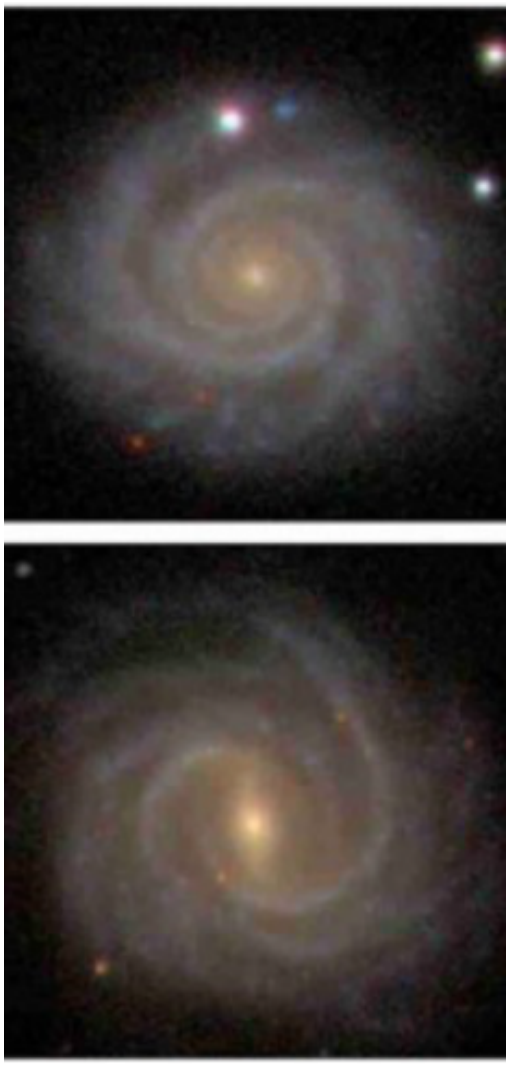

Figure 1.1: Left and right handed spiral galaxies [5].

Figure 1.2: Left and right handed spiral shells of snails [3].

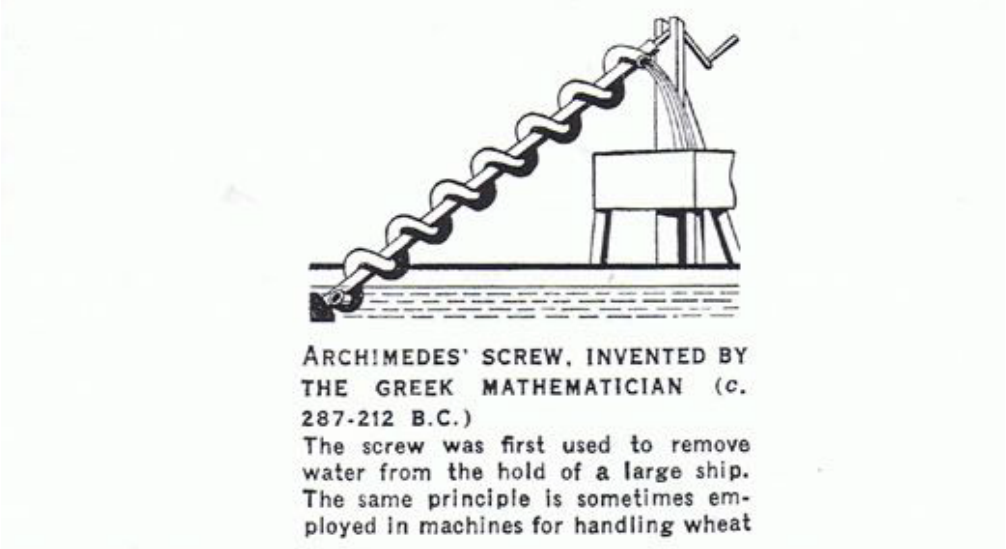

Figure 1.3: Archimedes screw displays chiral structure [6].

Also, chirality plays a role in odorants, for example, (4S)-(+)-carvone has a caraway scent, but (4R)-(-)-carvone has a scent of sweet spearmint Fig1.4. Our nose is a sensitive tool able to differentiate the two enantiomers. Human nasal receptors are chiral, which enables them to distinguish between these two enantiomers.

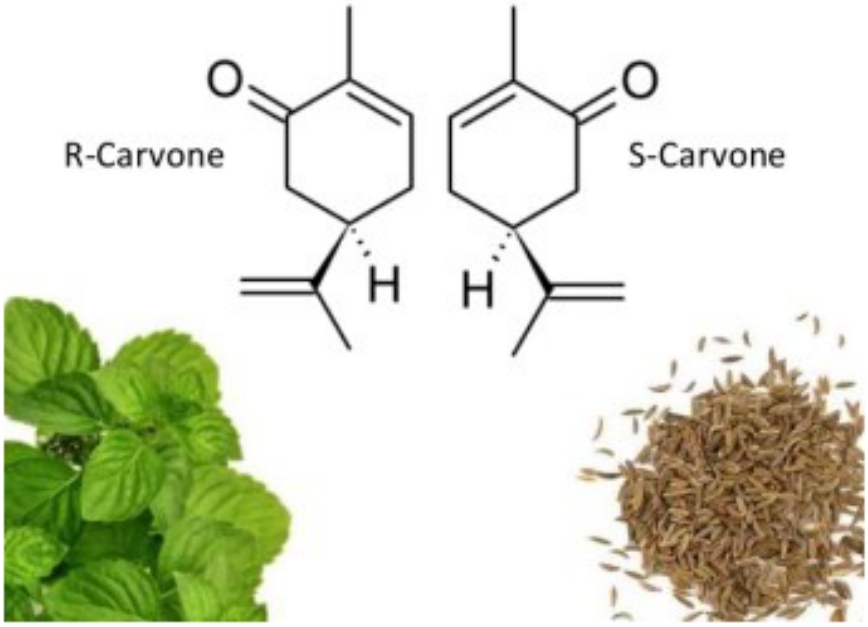

Figure 1.4: (S) and (R) enantiomers of carvone [7].

Accordingly, the left-handed and right-handed chiral molecules are called enantiomers. The two enantiomers have the same number of atoms, but they differ in their spatial arrangement [8]. They also have identical physical and chemical properties, yet they interact differently with chiral light or another chiral molecule [9]. Fig.1.5 depicts an example of a different arrangement of atoms in limonene ($C_{10}H_{16}$) ((S)-limonene, and (R)-limonene). (S)-limonene appears on the left side whereas (R)-limonene is on the right side. (R) stands for rectus in latin meaning: right, and (S) stands for sinister (latin: left). The ability to identify enantiomers is difficult due to the exact symmetry properties, including chemical properties and reactivity as well.

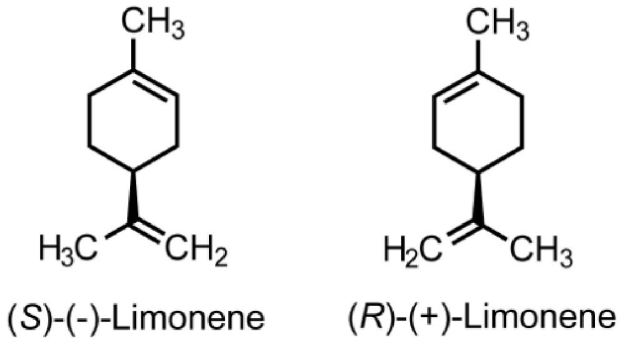

Figure 1.5: (S) and (R) enantiomers of limonene.

Chirality plays a vital role in pharmaceutical industries for developing drugs and in biochemistry. For instance, amino acids are chiral. They are the building blocks of living organisms on earth [10]. The enantiomers show differences in their pharmacology, toxicology, pharmacokinetics, and metabolism characteristics. Consequently, most of the developed drugs have been of specified chirality. Meaning that the chiral drug enantiomers interact differently with enzymes, proteins, and other chiral molecules. This fact leads to differences in the biological activities of the two enantiomers. The human body is selective in its responses to chiral components. One isomer may provide the desired effect, while the other may be ineffectual, and it maybe toxic. A well-known example is the drug labeled Thalidomide, which caused congenital disabilities. During the 1950s and 1960s, the drug was prescribed for pregnant women to reduce morning sickness. This drug was responsible for the birth of over 10,000 babies with deformations and disabilities as a result of the mothers taking Thalidomide during the first trimester of pregnancy, which prevents the proper growth of the fetus. The drug was of specified enantiomer but had low conversion threshold. Therefore, it changes to another enantiomer during a chemical reaction in the body [11]. Moreover,

chirality plays a significant role in biochemistry. Scientists acknowledge that two enantiomers of a molecule may contribute to different tastes and smells and other biological properties. For example, limonene enantiomers smell differently; the (R)-limonene smells like rose and (S)-limonene smells like turpentine [12]. These imply that the biochemical interactions of the two forms in the nose are different.

It has been more than 150 years since the discovery of chiral molecules, yet, studying chiral molecules is still a fascinating subject for scientists. In the 19th century, Louis Pasteur had demonstrated that many organic molecules in liquid form could rotate the plane of light polarization. Since then, studies of chiral molecules have been evolved rapidly. Furthermore, scientists and researchers have focused on developing new techniques to differentiate between chiral molecules at a single-molecule level. The optical rotation phenomenon explains the different responses of a molecule to right and left circularly polarized light. Section (1.2.1) provides a brief historical review about the discovery of optical rotation. The circular dichroism technique, which is the subject of section (1.2.2), is widely used to differentiate isomers. However, the severe drawbacks of this method led to the development of Photoelectron Circular Dichroism, which allows the study of molecules in gas phase to avoid solvent effects (further details in section (1.2.3)). In 2013, the Coulomb explosion method was used to study chirality (further details are in section (1.2.4)). Section (1.2.5) provides more information on the most recent technique used to study chirality, which is high harmonic generation.

Most of the known information about atoms and molecules comes from the interaction with light. The interaction of light with matter gives us the insight to understand

enantiomer structure and the ability to distinguish between them. Advancement in laser technology enable new techniques to study molecular interactions in an intense laser field including molecular photoionization that is capable of discriminating enantiomers via mass spectrometry. This thesis aims to understand and explore photoionization mass spectrometry to detect chirality.

This thesis describes the photoionization technique to study chiral molecules and distinguish them. This chapter discusses the commonly used methods for chiral discrimination and information about the strong field ionization mechanisms of atoms and molecules. Second chapter covers the description of femtosecond laser and the time of flight mass spectrometer used in the experiments along with the experimental method and setup. Chapter three focuses on explaining how the photoionization of a molecule as a function of elliptically polarized light is able to study the structure of the chiral molecule and discern them. Finally, chapter four presents future research in this field, along with the conclusion of this thesis.

1.2 Introduction to Chiroptical Methods

1.2.1 Optical Rotation

A linearly polarized light propgating in a chiral medium undergoes a rotatiotion about the optical axis [13]. The result of this rotation depends upon various parameters such as wavelength, concentration, path length and the configuration of chiral molecules. Optical activity

occurs only in chiral molecules. A racemic mixture will not rotate the polarization plane as each enantiomer will compensate the optical activity of the other, In 1811, Francois Arago observed for the first time, the phenomenon of optical rotation. He reported optical rotation in slabs of a crystal - quartz that was cut perpendicularly with respect to the optical axis and irradiated parallel to the optic axis [6]. In the year 1812, Jean-Baptiste Biot conducted subsequent experiments, he established that two forms of natural quartz exist which rotates the plane of polarization in opposite directions. He reported a calculation about the specific rotation $[\alpha]$ of a chiral analyte which is given by:

$$[\alpha] = \frac{\alpha}{CL} \tag{1.1}$$

where α is the angle of rotation, C the concentration of the solution in grams per milliliter and L is the path length in decimeters ($1dm = 10cm$).

He observed a decrease in the rotation of polarized light produced using a plate of quartz with a change of color from violet to red, i.e., shorter wavelengths are rotated more than the longer wavelengths. The phenomenon describing the dependence of specific rotation on the wavelength is called optical rotatory dispersion. In 1815, Jean-Baptiste Biot discovered that the rotation of linearly polarized light also occurs in liquids such as sugar solution and turpentine and it is not restricted to crystal substances [13]. Augustin Jean Fresnel developed the theory of optical rotation in the year 1824. He established the fact that linearly polarized light can be considered as the linear superposition of right and left circularly polarized (RCP and LCP) light with same frequency and amplitude. The index of refraction for LCP light and RCP light are different in a chiral medium. Therefore, the

rotation of the plane of linearly polarized light at a given wavelength in the optically active medium can be shown to be directly proportional to the difference in the refractive index. For one enantiomer [6]:

$$n_L(\lambda) - n_R(\lambda) = +\Delta n(\lambda) \neq 0, \tag{1.2}$$

and for the other:

$$n_L(\lambda) - n_R(\lambda) = -\Delta n(\lambda) \tag{1.3}$$

Where n is the refractive index and λ is the wavelength.

1.2.2 Circular Dichroism

For any molecule, absorption of light occurs at characteristic wavelengths. The strength of such an absorption is directly measured by the absorption coefficient (ϵ). In general, the light absorptions which are highly sensitive to the electronic structure of molecules lie in the ultraviolet-visible (UV/ VIS) wavelength range. An electronic transition corresponds to each absorption. This means that the electrons in the molecules are initiated by light of the corresponding wavelength, from an energetically lower (ground) to a higher(excited) state ($a \rightarrow b$). The difference in energy levels thereby taken up from the radiation field, $E_b - E_a$, which is related to the frequency of the exciting light ν, or the wavelength λ, by the well known Einstein-Planck relation:

$$E_b - E_a = h\nu = hc/\lambda \tag{1.4}$$

where h is Planck's constant, and c is the speed of light.

In chiral molecules, the nonzero difference of the refractive index for RCP and LCP light is

related to the fact that, inside absorption bands, the absorption coefficient for left and right circularly polarized light is also different: $\epsilon_l - \epsilon_R = \Delta\epsilon \neq 0$. This phenomenon is called circular dichroism (CD).

In 1849, Louis Pasteur was the first to show that optical rotation arises from chirality. He continued Biot's work of tartaric acid and its salts. He observed opposite optical rotations of tartaric acid salts. First, he separated crystals of this sample and solvated them separately in water, then he observed that one form rotates polarized light clockwise while the other form rotates the polarized light counterclockwise. A mixture of the two types of the sample was optically inactive and resulted in unrotated polarized light because the optical activity of one molecule cancelled the effect of the other molecule.

Circular dichroism has been used extensively to study chiral molecules. Chiral discrimination is achieved by left and right circularly polarized light. It is based on the small difference of absorption of left-handed (LCPL) and right-handed (RCPL) circularly polarized light over a range of wavelengths. It is well established that when circularly polarized light interacts with an optically active medium, there will be a difference in the extent to which they are absorbed $\epsilon_L \neq \epsilon_R$. Thus, when equal amount of LCPL and RCPL pass through the chiral molecule, one of these polarizations will be absorbed more than the other [14].

$$\text{circular dichroism} = \Delta A(\lambda) = A(\lambda)_{LCP} - A(\lambda)_{RCP} \tag{1.5}$$

ΔA is difference in absorbance, $A(\lambda)_{LCP}$ and $A(\lambda)_{RCP}$ are the absorbances for left and right circular polarized light as a function of the wavelength.

By applying Beer's law, eq.(1.5) can be written as:

$$\Delta A = (\epsilon_{LCP} - \epsilon_{RCP})CL \tag{1.6}$$

where ϵ_{LCP} and ϵ_{RCP} are the molar extinction coefficients for left and right circular polarized light, C is the molar concentration and L is the path length in cm.

CD occurs when the molecule has one chiral chromophore. Thus, left or right circularly polarized light will be absorbed to a greater extent than the other and the CD signal will be non-zero. The CD signal can be positive or negative depending on the absorption of CPL state. If left-handed circularly polarized light is absorbed to a greater extent than right-handed circularly polarized light, circular dichroism signal will be positive, whereas CD is negative when LCPL is absorbed to the lesser extent than RCPL [15] [16].

Quantum theory of light-matter interaction shows a direct connection between molecule's absolute configuration and its optical activity. Light absorption depends on evaluating the matrix elements between initial and final states of a radiation molecule operator. The cross section for a photon absorption process in which there is an electronic transition from an initial state $|i\rangle$ to a final state $|f\rangle$ [17]:

$$\sigma = 4\pi^2 \alpha_0 \hbar\omega \left\langle i|H_{int}|f\right\rangle^2 \delta(E_f - E_i - \hbar\omega) \tag{1.7}$$

where ω is the angular frequency, δ function represents the energy conservation, E_f represents the energy of the final state, E_i represents the energy of the initial state, α_0 is the fine structure constant, $\hbar$ is blank constant and H_{int} is the hamiltonian interaction. The scalar

product of the electron momentum P and the vector potential A of the radiation field is the interaction operator which is given as:

$$H_{int} = (\frac{e}{mc})\vec{P} \cdot \vec{A} \tag{1.8}$$

Where e and m are the charge and mass of the electron, resprctively and c is the speed of light. $\vec{A}$ is giving by:

$$\vec{A} = \vec{\varepsilon} e^{i\vec{k}\cdot\vec{r}} \tag{1.9}$$

where λ is the photon wavelength with wave vector $k = 2\pi/\lambda$ and $\vec{\varepsilon}$ is the polarization vector intacting with an electron at position r. The vector potential may be expanded in a truncated Taylor series which is given by:

$$e^{i\vec{k}\cdot\vec{r}} = 1 + i\vec{k} \cdot \vec{r} \ \text{ (provided that } \ \vec{k} \cdot \vec{r} \ll 1) \tag{1.10}$$

When eq (1.10) is substituted into the cross-section equation, it gives:

$$\sigma = 4\pi^2 \alpha_0 \hbar\omega \left\langle i|\vec{\varepsilon}\cdot\vec{P} + i(\vec{\varepsilon}\cdot\vec{P})(\vec{k}\cdot\vec{r})|f\right\rangle^2 \delta(E_f - E_i - \hbar\omega).(\frac{e}{m\cdot c})^2 \tag{1.11}$$

The $\left\langle i|\vec{\varepsilon}\cdot\vec{P}|f\right\rangle^2$ contribution of this term gives rise to the electric dipole absorption responsible for a large part of electronic spectroscopy. The second term in the matrix element can be further divided into antisymmetric parts and asymmetric, which are identified with magnetic dipole and electric quadrupole interaction operator in the following equation:

$$\begin{aligned}(\vec{\varepsilon}\cdot\vec{P})(\vec{k}\cdot\vec{r}) &= \frac{1}{2}[(\vec{\varepsilon}\cdot\vec{P})(\vec{k}\cdot\vec{r}) + (\vec{\varepsilon}\cdot\vec{r})(\vec{k}\cdot\vec{P})] + \frac{1}{2}[(\vec{\varepsilon}\cdot\vec{P})(\vec{k}\cdot\vec{r}) - (\vec{\varepsilon}\cdot\vec{r})(\vec{k}\cdot\vec{P})] \\ &= \text{ electric quadrupole} + \text{ magnetic dipole}\end{aligned} \tag{1.12}$$

In the expansion of the transition operator, the presence of the higher-order terms results in further contributions to the absorption cross-section. Their contributions are expected to

be smaller than the electric dipole contribution in many ways, due to their dependence on power of $k \cdot r$. Generally photon-molecule interaction is expanded as the transition operator in a series with electric and magnetic multipole contributions:

$$\begin{aligned} T &= E_1 + E_2 + E_3 + ... + M_1 + M_2 + M_3 + ... \\ &= \text{electric dipole} + \text{electric quadrupole} + \text{electric octupole} + ... \\ &+ \text{magnetic dipole} + \text{magnetic quadrupole} + \text{magnetic octupole} + ... \end{aligned} \quad (1.13)$$

These multipoles behave as tensors of increasing rank (k) and alternating parity given by $(-1)^k$ for electric moments and $(-1)^{k-1}$ for magnetic moments. Therefore, each of these transition probability amplitudes (channels) will contribute to the total transition probability. Also, there will be contributions from each cross-term which involves transition moment operators of opposite parity. This process explains the origin of CD as it gives rise to the differential absorption of circularly polarized light. The interference of the magnetic and electric dipole transition amplitudes (the $M_1 - E_1$ mechanism) which is also expressed as the rotational strength [18] in the Rosenfeld-Condon equation, is defined as the pseudoscalar product of the electric and magnetic dipole transition:

$$R_{if} = Im\{\langle i|\mu|f\rangle \cdot \langle f|m|i\rangle\} \quad (1.14)$$

where μ is the electric dipole moment operator and m is the magnetic dipole moment operator of the molecule. When absorbance phenomena are described, μ, m should be interpreted as operators. Im stands for imaginary quantity. If there is no external magnetic field, the initial and final states should be real wavefunction. μ and m are real vectors and m describes the rotation in the Gaussian coordinate system of complex number.

Notice that the rotational strength expression eq(1.14) is a dot product between electric (μ) and the magnetic (m) dipole operators. It applies only for a molecule in an isotropic medium. A pseudoscalar quantity is a rotational invariant but, unlike a true scalar, it has odd parity, therefore it inverts its sign between enantiomeric system. Since the rotational strength [18] is a dot product of two different transition moment vectors, it can be either a positive, negative or zero. If these two vectors are parallel, this leads to a positive sign and antiparallel leads to negative. Only in a chiral system, the rotational strength value is non zero, and it vanishes in achiral system [19]. Occasionally, when a transition is nominally electric dipole forbidden but magnetic dipole allowed, as in the $n \rightarrow \pi^*$ excitation of carbonyl groups, larger percentage asymmetries are obtained because the interfering terms become commensurate with one another. The electric dipole transitions are identical in the two enantiomers, whereas, the magnetic dipoles are pointing in opposite directions leading to opposite dynamical electronic response in the two enantiomers. Thus, the electric dipole is not enough to explain the CD results and a higher order contribution is needed.

The electric dipole transition moment which occurs on the transition from the initial state i to the final state f can be defined as a linear displacement of a charge. The electric field of the light induces transitions through coupling with μ, if the photon energy matches the energy difference between the two states. The magnetic dipole transition moment is known as the measure of the circular motion of charge associated with $i \rightarrow f$ transition. Thus, magnetic dipole transitions depend on the field direction and this field direction changes when left and right handed polarized light are used, nevertheless, the electric dipole transition is

independent of the light handedness [20]. To give rise to CD, a transition must involve both linear and circular charge movement, with the axis about which circular motion occurs having a component along the direction of linear displacement. This combination of linear motion along an axis with circular motion around the axis corresponds to a helical displacement of charge. The sense of helix is determined by the relative signs of μ and m. The probability for a transition to occur between two different atomic states depends on the matrix element linking these states. The most probable transitions are known as electric dipole transitions. These transitions are allowed when the electric matrix element is non zero $\mu_{if} \neq 0$, if $\mu_{if} = 0$, it is a forbidden transitions .

$$\mu_{if} = -\langle i|x|f\rangle \tag{1.15}$$

where x is the position vector of the particle and this term is non zero only if: $\Delta L = \pm 1$, $\Delta m = 0, \pm 1$, $\Delta m_s = 0$. L is the azimuthal quantum number, m is the magnetic quantum number, and m_s is the spin quantum number. $\Delta m_s = 0$ because $\mathbf{x}$ does not explicitly depend on spin.

These are the selection rules for electric dipole transitions. Transitions which are forbidden at the electric dipole level may still occur, if the magnetic dipole transition matrix element $m_{if} \neq 0$,

$$m_{if} = \langle i|L + 2S|f\rangle\,, \tag{1.16}$$

where L is the orbital angular momentum, and S spin angular momentum.

Magnetic dipole transition will be allowed only if the magnetic dipole matrix element is non-zero, and that occurs only if $\Delta L = 0$, $\Delta m = \pm 1$, $\Delta m_s = \pm 1$. These are the selection rules for magnetic dipole transitions.

Randomly oriented samples absorption measurements provide a very small dichroism difference signal. The chirality induced asymmetry is known as Kuhn's g-factor [17], which defined as the ratio of absorbances or molar absorptivities:

$$g = (A_L - A_R)/(A_L + A_R) \tag{1.17}$$

Kuhn's dissymmetry g-factors rarely exceed 0.01% making them a challenging quantity to measure. Consequently, the technique is always applied to non-dilute samples in the liquid phase. The usable wavelengths are commonly restricted by the availability of transmission polarizing optics ($\lambda/4$ wave plates) to the region $> 110nm$, and are usually further restricted by solvent absorption to $> 160nm$.

This technique has its limitation. First, the circular dichroism effect is weak (CD signals of $=10^{-5} - 10^{-4}$) which required to perform the measurement in solution [21]. Second, because of the low number density, a measurement in the gas phase cannot be done. This led to the development of a new method, which is photoelectron circular dichroism.

1.2.3 Photoelectron Circular Dichroism (PECD)

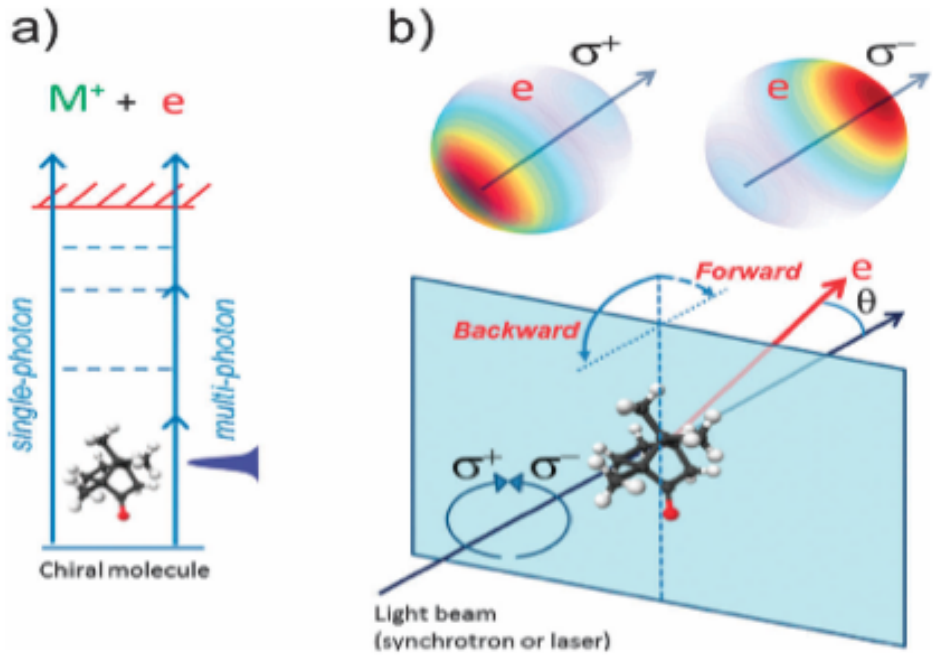

Figure 1.6: a) Single-photon and multiphoton ionization, b) illustration of photoelectron circular dichroism measurement. The angular distribution of photoelectrons is imaged after photoionization with either left or right circular polarized light. (θ) is the angle between the direction of the circular polarized light beam and the velocity of the electron. The photoelectron angular distribution of a chiral molecule demonstrates a forward–backward which switches sign based on the handedness of the molecule. Image and caption are reproduced with permission from Royal Society of Chemistry [21].

Photoelectron circular dichroism is a highly sensetive technique to differentiate and recognize chiral molecules in a gas phase since it depends only on pure electric dipole transitions. In PECD, the photoionization of the chiral molecule can be done by using ultra-fast pulses or the synchrotron source along with the impact of the circularly polarized light, which causes the emission of the photoelectrons' angular distribution. For right-handed and left-handed circularly polarized light, the electrons distribution is different. Fig.1.6 shows that the photoelectron angular distribution, referred to as PAD, exhibits a forward-backward asymmetry that is typical for the direction of the light propagation. The asymmetry is zero for a racemic mixture or achiral molecules. Depending on the polarized light's handedness as well as the type of chiral molecule, the asymmetry changes its direction [22].

In a single-photon ionization, the photoelectron flux angular distribution I(θ) is given based on the following equation, [23],:

$$I_{\{p\}}(\theta) = 1 + b_1^{\{p\}} P_1(cos\theta) + b_2^{\{p\}} P_2(cos\theta) \tag{1.18}$$

In this expression, P_1 represents the first order Legendre polynomial. The values $b_1^{\{p\}}$ and $b_2^{\{p\}}$ depend on the polarization and the photoionization dynamics. θ is the angle between the vector of the electric field and the direction of the electron. The polarization is expressed through the p superscript, which takes the value 0 when the polarization is linear and takes the value ± 1 when the circular polarization is left or right. These coefficients have the following characteristics and properties:

$$b_1^{\{0\}} = 0 \tag{1.19}$$

$$b_1^{\{+1\}} = -b_1^{\{-1\}} \tag{1.20}$$

$$b_2^{\{\pm 1\}} = -(1/2)b_2^{\{0\}} \tag{1.21}$$

The second term of eq (1.18) gives rise to the enantio-selectivity. Since $b_1^{\{p\}} = 0$, the term $b_1^{\{p\}} P_1(cos\theta)$ does not show sign variation for linear polarization. For circular polarization, the second term is anti-symmetric since $b_1^{\{+1\}} = -b_1^{\{-1\}}$. It changes sign when exchanging either the incoming polarized light or the enantiomer. The third term does not have a sign dependence even for circularly polarized light because $b_2^{\{\pm 1\}} = -(1/2)b_2^{\{0\}}$.

By applying equation (1.19) on (1.18), the first term P_1 will vanish and an expression that applies for linear polarization will be obtained:

$$I_{lin}(\theta) = 1 + \beta P_2(cos\theta) \tag{1.22}$$

The parameter of anisotropy is β, which is equal to $b_2^{\{0\}}$. P_2 is the second term of the Legendre polynomial, which introduces the anisotropic term, which takes values that vary within the ranges between $\sin^2\theta$ and $\cos^2\theta$. $b_1^{\{p\}} = 0$ is a general restriction for the achiral molecule, which applies to all polarizations. In the case of $b_1^{\{\pm 1\}}$, the non-zero value is only possible to obtain for chiral molecules and circular polarization. Therefore, the anticipation of the forward–backward asymmetry within the angular distribution is possible as the θ angle between the electric field vector and the electron direction, rotates to 180°. When the helicity of the radiation is exchanged, the anti-symmetric nature of the coefficient $b_1^{\{\pm 1\}}$ (eq(1.20)) causes difference between the response to left and right-handed circular polarization in the angle resolved photoelectron spectrum. This process leads to the generation of the circular dichroism or it may lead to the rise of the difference in the angle resolved photoelectron spectrum response to the left-handed or the right-handed circular polarization. When the enantiomeric

molecular target's handedness is exchanged or switched, we may obtain a similar reversal.

The forward–backward asymmetry in photoelectron distribution may occur when a randomly oriented sample of molecular enantiomers is ionized using the circularly polarized light. The photoelectron angular asymmetry is the variation in the fluxes of the electron throughout the elements of the area, represented by $\sin\theta d\theta d\phi$. These differences occur on the sphere going from 0° and 180° as ratioed to the average flux throughout the element of the area.

$$G_{AD} = [I_p(0^\circ)\sin\theta d\theta d\phi - I_p(180^\circ)\sin\theta d\theta d\phi]/\sin\theta d\theta d\phi \tag{1.23}$$

$$G_{AD} = 2b_1^{\{p\}} \tag{1.24}$$

where G_{AD} is the asymmetry factor. The coefficient $b_i^{\{p\}}$ gives rise to the forward-backward electron emission asymmetry with respect to the direction of the light propagation. This coefficient is non-zero only in the case of chiral molecules subject to circular polarized light. The asymmetry is the difference between the flux of the electron for CPL of opposite handedness. From Eq. (1.18) and the antisymmetry property of Eq. (1.20) one obtains an expression for the PECD:

$$I_{LCP}(\theta) - I_{RCP}(\theta) = (b_1^{\{+1\}} - b_1^{\{-1\}})P_1(\cos\theta) = 2b_1^{\{+1\}}\cos\theta \tag{1.25}$$

The PECD measurement clearly takes the form of a cosine function with an amplitude given entirely in terms of the single chiral parameter, b_1. It therefore provides exactly the same information content as the G asymmetry factor defined above [Eq. (1.24)]. The electron's angular distribution asymmetry in PECD is attributed to electric dipole transitions happening within the process of ionization. Therefore, the asymmetry's magnitude is large ranging

between 1% and 10%. This asymmetry magnitude is larger by many orders of magnitude than that related to the conventional method (CD) due to the fact that the magnetic dipole is significantly weaker than the electric dipole transition (typically less than 0.01%) [21]. It is important to note that PECD is commonly present and abundant in the pure electric dipole approximation, which is not the case of the conventional method requiring weak magnetic interactions or electric quadrupole along with high order.

1.2.4 Coulomb Explosion

For a long time, scientists did not have any method that could directly measure and account for the handedness and the molecular structure. The use of the Coulomb explosion enables the measurement of the absolute configuration in a gas phase. This technique relies on the use of intense femtosecond laser pulses at high repetition rate (100 kHz), which results in multiple ionization and followed by the fragmentation in a process called Coulomb explosion. During this process, the strong femtosecond laser pulse causes the molecule to break into different fragments. The time of the arrival and the position of each of the fragment ions are detected. From the momentum of each fragment ion one can reconstruct the molecular structure.

According to Pitzer et al (2013); the authors used the Coulomb explosion along with the COLd Target Recoil Ion Momentum Spectroscopy (COLTRIMS) to find the absolute configuration of CHFClBr. They were also able to separate the enantiomer using these

tools [25]. They used a high repetition rate (100 kHz) femtosecond laser to generate multiple ionization causing the Coulomb explosion to occur. The fragmentation process resulted in the formation of $(Br^+, Cl^+, F^+, C^+, \ and \ H^+)$. The ion imaging determines the time of arrival and the position where the fragment hits the detector, which consequently allows the absolute configuration to be determined. From the position of the fragments on the detector, the distance between the MCP and the ionization zone, and the time-of-flight, all cation velocities can be obtained. From this detection of the absolute value of the linear momenta of the detected particles is possible.

The advantage of this method is that it allows the identification and determination of the two enantiomers within the racemic mixture. In addition, it gives information about chirality on a single molecule level, which makes this process of interest for studying the fundamental of chiral molecules and to analyze chiral mixture. However, this method does have its drawbacks in cases where complicated and large molecules make it tough to detect all the fragments present within the stereocenter. Moreover, the likelihood of detecting multi-fragments in coincidence decreases significantly as the number of atoms in the molecule increase.

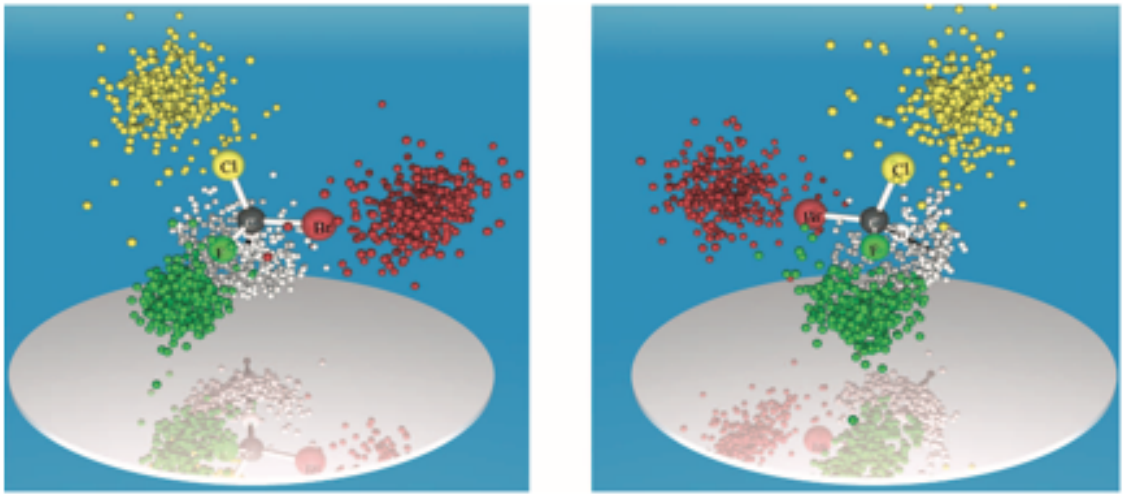

Figure 1.7: The linear momenta of $CHFClBr$ enantiomers are plotted for $(S)-CHFClBr$ (left) and $(R)-CHFClBr(right)$. Image and caption are repreduced with permission from Royal Society of Chemistry [26].

1.2.5 High Harmonic Generation (HHG)

High harmonic generation is an extremely high order nonlinear process. This technique can produce spatially and temporally coherent light. It is also capable to generating short pulses of about a hundred attoseconds. HHG can be achieved by focusing an intense laser field into a gas or solid. The HHG process consists of three steps: 1) the electron photoionization in a strong field, 2) the acceleration of the liberated electron in the laser field, and 3) the recombination, all within one laser cycle. These three steps are illustrated in Fig.1.8, which is known as the three-step model.

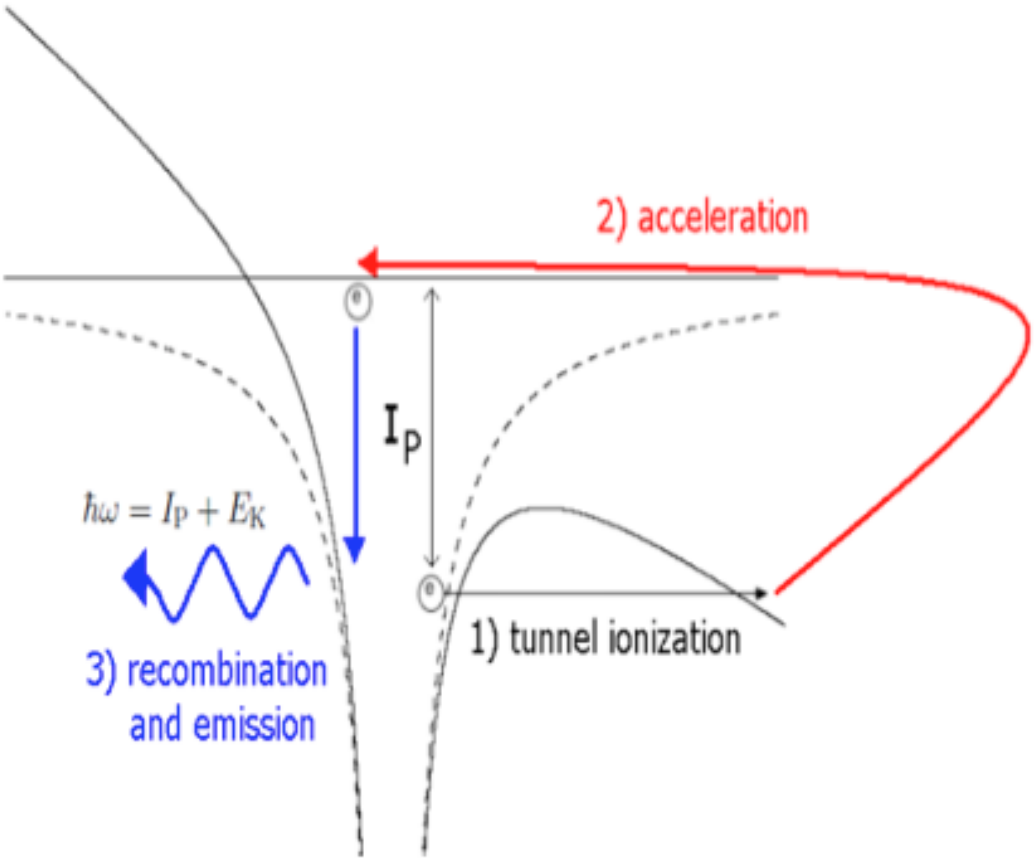

Figure 1.8: Shows the three steps of high harmonics generation [27].

Explicitly, electron photoionization results from the distortion of the atomic potential of the molecule by a strong laser field followed by the electron tunneling into the continuum. Second, under the influence of electric field of the laser, the freed electron accelerates moving outward from the parent molecule and gaining energy. Depending on the shift in polarity of the electric field, the electron returns and recombines with the parent ion resulting in XUV photon emission. A typical spectrum of HHG involves a 'perturbative' region, followed by a 'plateau' and a 'cut-off' as shown in Fig.1.9

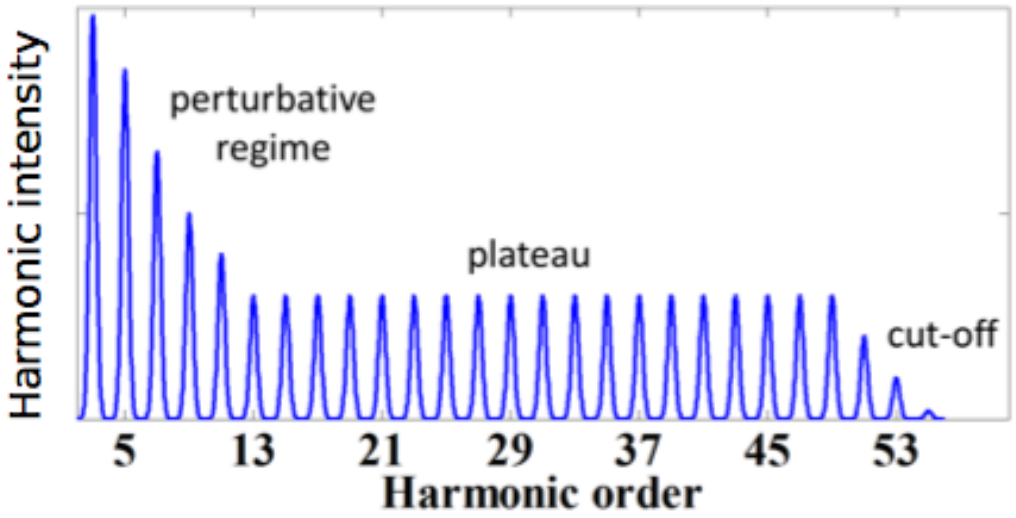

Figure 1.9: Spectrum of high harmonic generation [28].

In achiral molecules, the HHG yield spectrum is a symmetric Gaussian function of ellipticity ϵ, with its maxima at $\epsilon = 0$. As ϵ increases, HHG yield decays quickly because, in an elliptical driving field, the liberated electron acquires a lateral drift that increases as the ϵ increases. At $\epsilon \geqslant 20\%$, the electron that is accelerated by the laser misses the parent molecule. Consequently, it quenches electron-hole recombination, therefore decrease in the HHG yield. However, the results show that the HHG yield is asymmetric in a gas consisting of randomly oriented chiral molecules, with its maximum at $\epsilon \neq 0$. The HHG exhibits elliptical dichroism.

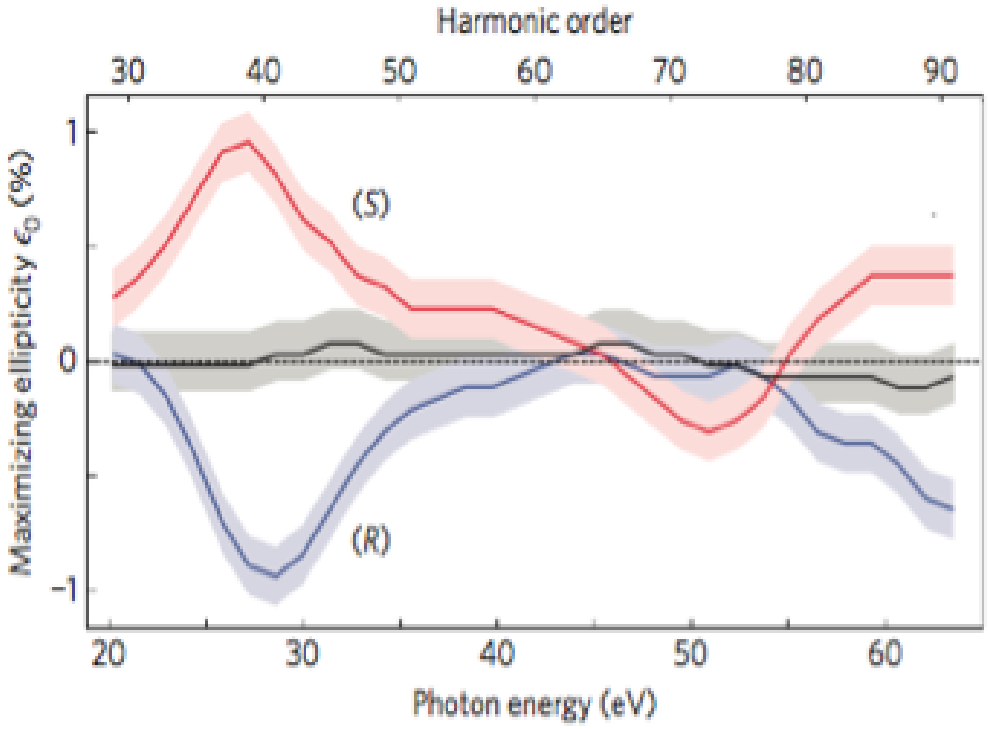

Figure 1.10: Measurement of propylene oxide enantiomers using HHG as a function of laser ellipticity. For each harmonic order, the corresponding ellipticity dependence is fitted with a Gaussian function, the central position of which we call maximizing ellipticity ϵ_0. ϵ_0 is shown as a function of the harmonic order (top axis) and the emission energy (bottom axis). Red and blue traces correspond to enantiomers of propylene oxide. The black line shows the non-chiral reference (xenon). The measurements were taken at 1770 nm, with intensity $5 \times 10^{13} W/cm^2$. Image and caption are reproduced with permission from Nature [29].

The HHG physical process is the result of the dipole approximation in which all the effects of the magnetic field are neglected. In the dipole approximation, as the E-field polarity is the same in both (R) and (S) molecules, the chiral dichroism is absent in high harmonic emission. In contrast, upon reflection, the magnetic field changes its direction in

the plane of polarization, making the microscopic interaction naturally chiral. In the HHG process, the magnetic field of the laser acts further on: i) the liberated electron, ii) the ionic core of the parent ion. This process may lead to the following two types of mechanisms:

In type I, the laser magnetic field acts on the freed electron. Subsequently, the electron moves outward of the polarization plane due to the Lorentz force. The elliptical polarization causes the electron trajectory between ionization and recombination to become chiral. Also, the recombination of the freed electron with the chiral parent ion results in the process of chiral discrimination.

In type II, the magnetic field of the laser acts on the parent ion inducing transitions between the excited states. This process depends on the sign of the magnetic dipole, which is opposite for the two enantiomers. Therefore, HHG, in this case, is affected by the sign of the helicity [29]. The chiral-sensitive transitions in the parent ion cause the type II mechanism. It corresponds to the ionization from one orbital and recombination to another orbital. Further, it requires moving the hole between orbitals via the laser field on a sub-laser cycle timescale.

In propylene oxide, the ion ground state ($\tilde{X}$) concurs with the removal of the lone pair electron from the out-of-plane p orbital of the oxygen atom. The first excited state($\tilde{A}$), which corresponds to electron removal from another oxygen lone pair, further stabilized by

partial involvement in the $C-O$ bonds. Ionization under the influence of the intense laser field produces both ($\tilde{A}$), and ($\tilde{X}$) states with equal efficiency, which opens two main HHG channels, (XX) and (AA) eq(1.26). The first letter denotes the ionization channel, whereas the second letter identifies the recombination channel. For instance, (XX) indicates ionization into the $\tilde{X}$ ionic state. It also implies the freed electron recombination with the same $\tilde{X}$ ionic state. Also, no magnetic-dipole transitions in the ion are involved in these 'direct' channels, hence carry no chiral signal. However, in the ion, laser-induced transitions occur between ionization and recombination, which causes the opening of two additional cross-channel (AX and XA). Accordingly, the 'AX' channel is related to the ionization process happening within the $\tilde{A}$ state while the recombination process happen within the $\tilde{X}$ state. Both states are enabled by the $\tilde{A}\rightarrow\tilde{X}$ transition that occurs between ionization and recombination within the cation. The cross-channels (XA) that involve magnetic-dipole transitions and are thus inherently enantiomer selective.

$$\begin{aligned}\overline{d(N)} &= \overline{d_{\tilde{X}\tilde{X}}(N)} + \overline{d_{\tilde{A}\tilde{A}}(N)} + \overline{d_{\tilde{X}\tilde{A}}(N)} + \overline{d_{\tilde{A}\tilde{X}}(N)} \\ &\simeq \overline{d_{\tilde{X}\tilde{X}}(N)} + \overline{d_{\tilde{A}\tilde{A}}(N)} + \overline{d_{\tilde{A}\tilde{X}}(N,\theta_{max})} \\ &= \overline{d_{\tilde{A}\tilde{A}}(N)}[[1+R_{\tilde{A}\tilde{X}}]e^{iE_{\tilde{A}\tilde{X}}\tau(N)} + R_{\tilde{X}\tilde{X}}]\end{aligned} \tag{1.26}$$

where the first term represents the ionization from $\tilde{X}$ state and recombination to $\tilde{X}$ state, second term corresponds to ionization from $\tilde{A}$ state and recombination to $\tilde{A}$ state. These two terms does not contribute to the magnetic dipole transitions. The third and fourth terms are the interference terms that involve magnetic dipole transitions. θ_{max} corresponds to the solid angle. The direction of ionization from $\tilde{X}$ and recombination to $\tilde{A}$ changes by θ_{max} that improve the ionization into the $\tilde{A}$ and recombination into the state $\tilde{X}$. $E_{\tilde{A}\tilde{X}}$

corresponds to the energies difference between ($\tilde{A}$ and $\tilde{X}$) states. $\tau(N)$ represents time lag between ionization and recombination. $R_{\tilde{A}\tilde{X}}$ is the cross channel amplitude and $R_{\tilde{X}\tilde{X}} \simeq 1$.

The issue with HHG is that it is a complex process, forming a three step sequence: ionization via MPI or tunneling, propagation in the laser field, and recombination. The aim of this thesis is to perform a more straightforward and effective method to achieve chiral discrimination from only the process of photoionization.

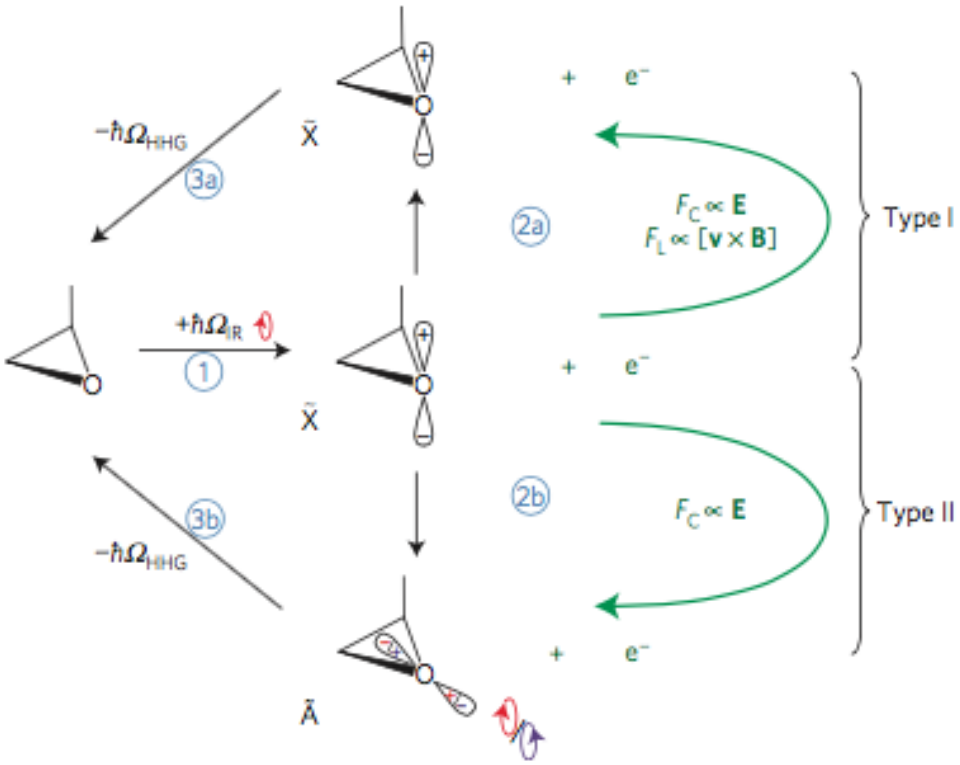

Figure 1.11: Mechanisms of chiral sensitivity for high-harmonic emission. Type I: (1) Tunnel ionization of a neutral molecule produces an electron e^- and a molecular cation in its ground state ($\tilde{X}$); (2a) The electron is accelerated by the laser electric field (E) and acquires chiral displacement due to the action of the Lorentz force (v × B) ; (3a) The electron recombines with the ion, emitting an energetic photon. Type II: (2b) The ion undergoes sub-cycle electric- and magnetic-dipole transitions, which change the ionic state (for example, $\tilde{X} \rightarrow \tilde{A}$) between ionization and recombination and open chiral-sensitive HHG channels XA and AX; (3b) Recombination leads to emission of an XUV photon. The interference between the chiral-sensitive HHG channels XA and AX and the non-chiral HHG channels XX and AA associated with ionization and recombination to the same orbital leads to homodyne enhancement of the chiral signal. Image and caption are reproduced with permission from Nature [29].

1.3 Introduction to Strong Field Physics

In this section, background information related to the light-matter interaction in strong field regime will be explained in detail. It addresses the physics behind the mechanisms of strong laser field ionization including, multiphoton ionization, tunneling ionization and Keldysh parameters. Ionization is an important and fundamental process for many technologies, such as mass spectrometry which depends highly on the ionization phenomena. According to the photoelectric effect, when the photon energy exceeds the binding energy of electron also known as ionization potential, electron separates from the atom or process of ionization occurs (single photon absorption).

Strong laser field ionization can be described via two regimes, multi-photon ionization and tunneling ionization. Both of these regimes are discussed in the following sections.

1.3.1 Multiphoton Ionization

Atomic photoionization takes place when the energy of the photon is higher than or equal to the ionization energy of an atom. However, if the photon flux is strong enough, photons with an energy ($h\nu$) (much less than the ionization energy E_i of an atom) can ionize an atom with an ionization energy E_i. In order to ionize an atom, the atom must absorb several photons from the laser radiation. In other words, multi-photon ionization occurs when an electron is ionized by absorbing N photons and gains enough energy to move to the continuum. Multiphoton processes are defined by the energy time uncertainty principle, $\Delta E \Delta t \geq \hbar$. This principle permits the system to pass through virtual states for Δt given an

energy uncertainty of ΔE. Second photon absorption depends on it arriving within the time Δt. Then, the system can make a transition to the "two photon" absorbed state effectively. Likewise, the next photon absorption depends upon the arriving of the third photon before the atom or molecule de-excitation.

The probability of multiphotoionization is based on the photon energy and decreases with increasing the number of photons that are required for the process. The probability of absorbing multiple photons depends on the laser intensity and the MPI probability becomes smaller when the number of absorbed photon increases based on the following relation

$$R_n = \sigma_n I^n \tag{1.27}$$

where R_n is the probability of absorbing n photons, I is the intensity of incindent light, σ_n is generalized cross section, n is the number of photon ionizaton.

In MPI the laser electric field is small in comparison with the intraatomic field. MPI can be observed at light intensities ranging from $10^{12} W/cm^2$ to $10^{14} W/cm^2$ with 800nm wavelength. At longer wavelengths, tunneling becomes more pronounced as described in section (1.3.2).

1.3.2 Tunneling Ionization

Tunnel ionization is a quantum phenomenon. Under the influence of intense laser field, an atomic or molecular potential is suppressed allowing the electron to escape to the continuum. With sufficient electric field intensity at low enough frequency, where the targeted electron has sufficient time to transit through the molecule‘s potential barrier, the Coulomb potential barrier will be distorted radically. The Coulomb potential barrier is deformed and lowered

to allow the electron to tunnel through the barrier and escape from the atom or molecule, as shown in Fig.1.12b. By applying a higher laser intensity or having a molecular target with lower ionization potential, the potential barrier is lowered more and the tunneling ionization becomes more probable. As the electric field is increased, the barrier becomes smaller and lower until the ground state is unbound eventually leading to over barrier ionization. The ionization probability becomes one, and Coulomb potential suppresses completely as illustrated in Fig. 1.12c

$$\mathbf{I}_{OTBI}[W/cm^2] = 4 \times 10^9 (I_p[eV])^4/Z^2 \tag{1.28}$$

Both ionization regimes (MPI and tunneling) are controlled by the Keldysh parameter which is explained in detail in section (1.3.3).

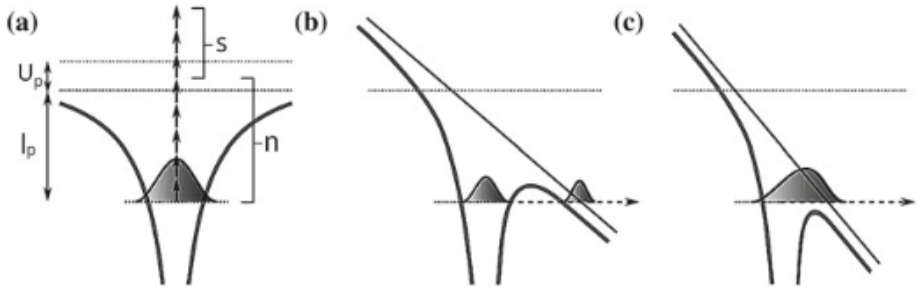

Figure 1.12: Schematic diagram showing the three mechanisms for ionization a) multiphoton ionization dominates at low intensity, b) tunneling ionization occurs when the intensity is increased, therefore Coulomb potential is distored, c) at even higher intensity the Coulomb potential is supressed completely, permitting the electron wavepacket to escape freely. This is over barrier ionization [30].

.

1.3.3 Keldysh Parameter

In 1964, Keldysh showed for the first time that the multiphoton ionization and tunneling process are the two cases of nonlinear photoionization. Both of these regimes depend strongly on Keldysh Parameter γ which depends on the ponderomotive potential U_{pond}, which can be written as:

$$\gamma = \sqrt{I_p/(2U_{pond})} \tag{1.29}$$

where U_{pond} is the ponderomotive energy and given by:

$$\mathbf{U}_{pond} = e^2E^2/(4m\omega^2) \tag{1.30}$$

where ω is the laser frequency, e and m are the charge and mass of the electron respectively, E is the electric field strength.

The ponderomotive potential describes the oscillation energy of a free electron in the electric field. Also, it can be expressed in electronvolt as

$$\mathbf{U}_{pond} = 9.33 \times 10^{-14} I\lambda^2 \tag{1.31}$$

where I is in W/cm^2 and λ is in μm.

When the Keldysh parameter is greater than one ($\gamma > 1$) MPI occurs [31]. When the Keldysh parameter is less than unity ($\gamma < 1$), the field is strong enough to depress the Coulomb potential allowing the electron to tunnel and escape from the atom or molecule. Keldysh parameter is essentially the ratio of laser and tunneling frequencies.

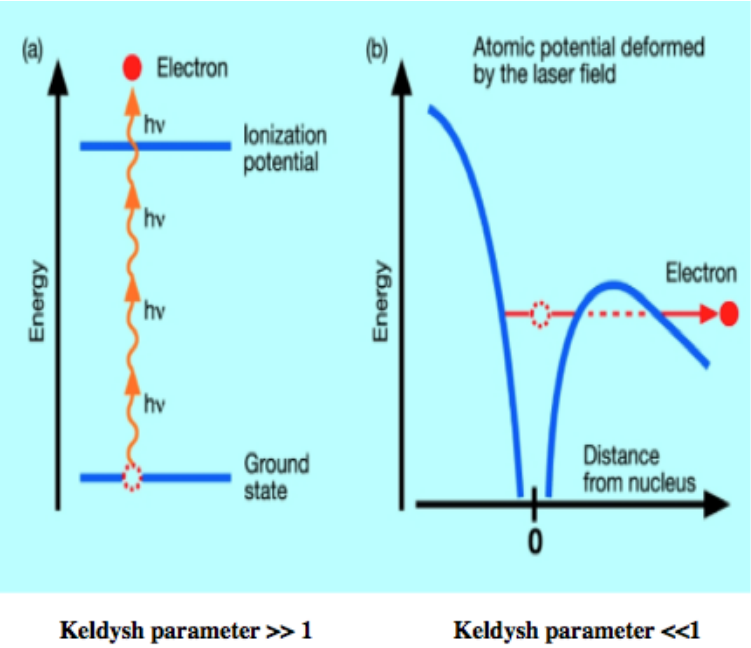

Figure 1.13: Shows the different regieme according to Keldysh parameter. Image is reproduced with permission from [32].

1.3.4 Sequential and Non-Sequential Double Ionization

As mentioned in the previous section, there are two ionization regimes (MPI) and tunneling. In both regimes the electron escapes from the atom or molecule to the continuum. However, after the electron is ionized further ionization could occur under certain conditions giving rise to possible mechanisms: sequential and non-sequential ionization. Under strong electric laser field, the laser field will be intense enough to ionize the molecule multiple times directly. This process is known as sequential double ionization (SDI).

$$A + nh\nu \rightarrow A^{+} + e^{-} \tag{1.32}$$

$$A^{+} + nh\nu \rightarrow A^{++} + e^{-} \tag{1.33}$$

In addition to ionizing the electron directly, a non-sequential double ionization (NSDI) process can occur. The process begin with the molecule absorbing energy and ionizing an electron. Upon ionization, the liberated electron propagates in the continuum under the influence of the laser field and gains energy by a factor of $3.17U_{pond}$, U_{pond} is the ponderomotive energy. The freed electron can recoillde with the parent ion resulting in one of the three phenomena: elastic scattering, recolliding with another electron or recombining with parent ion depending on the laser field polarization. In NSDI, the ionized electron propagates in the laser field, then re-collides with the parent ion ejecting a second electron as illustrated in Fig. 1.14

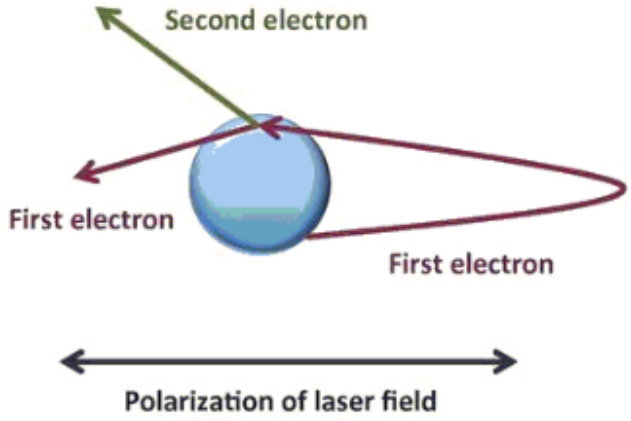

Figure 1.14: Electron recollosion with the parent ion resulting in nonsequential double ionization.

Non-sequential ionization depends highly on the laser polarization, since laser polarization can control the electron trajectory which influences the probability of re-collision. Therefore, SI and NSDI processes can be distinguished by varying the laser polarization. For example, for circular polarization, NSDI vanishes because the electron is driven away from the parent ion core, however, both of these two regime are active for linear polarization.

For linear polarization, the kinetic energy of the re-collide electron must exceed the second ionization of the parent ion. However, by varying the ellipticity of the laser polarization, the electron misses the parent ion core, therefore the amount of overlap between the returning electron and the parent ion can be controlled.

These two process are important to interpret the photoionization results because of their contribution to the overall yield. SI and NSDI acting together is the reason for the presence of the doubly charged molecules. Their contribution can be distinguished by varying the ellipticity of laser polarization.

1.4 Elliptical Polarization Variation

The ellipticity of a laser beam is defined as the ratio of minor (y) to major (x) of the electric field, that is $\epsilon = E_y/E_x$. Polarization variation gives us information about the transverse electron momentum of the tunneled electron wavefunction, because the electron wavepacket will have an initial transverse velocity. During the propagation in the laser field, the electron wavepacket returns to the parent ion leading to possible recollision depending on this transverse momentum. Linearly polarized light usually gives the maximum probability for recollision as the electron wavepacket is returned directly to the parent molecule. When ellipticity is increased, the electron wavepacket is increasingly brought further away from the ionization center point. As circular ionization is reached, the electron wavepacket misses (exceeds the radius of the molecular ion) the parent ion completely, because E_x and E_y are equal.

The transverse spread of the tunneled electron wavefunction is measured by varying the laser polarization. The electron is accelerated away from the parent ion but as the laser field reverses, the electron is driven back resulting in possible recollision. Depending on the transverse momentum, the electron can re-collide with its parent ion. Thus, the distribution of transverse momentum of the tunneled electron depends on the strong field processes and ionization potential which can be expressed as [33]:

$$\psi(P_\perp) = \psi(P_\perp = 0)e^{-P_\perp^2\sqrt{2I_p}/E} \tag{1.34}$$

where $\psi(P_\perp)$ is the distribution of transverse momentum of the tunneled electron.
$P_\perp$ is the initial transverse momentum of the electron, I_p is ionization potential and E the electric field of the ionizing laser pulse at the moment of tunneling.

We can discern this based on the variation of doubly charged ions resulting from Non-Sequential Double Ionization. For argon, ellipticity variation of ion yield is expected to have a Gaussian distribution with a maximum at linear polarization, falling off sharply as ellipticity is increased toward a value of 1 as seen in Fig 1.15:

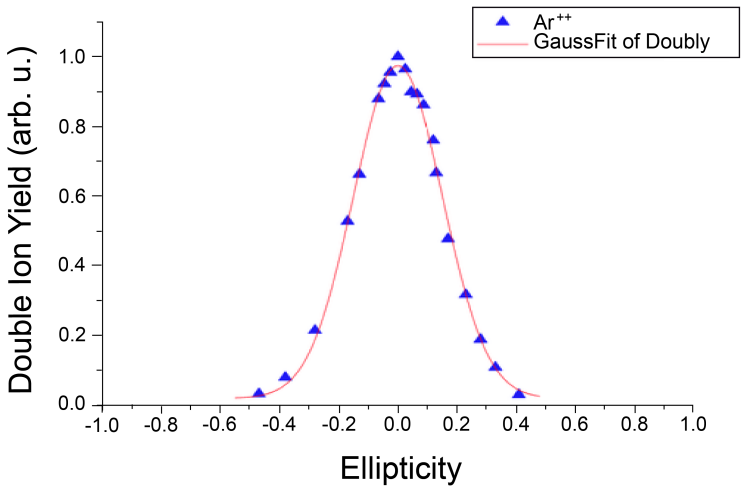

Figure 1.15: Shows argon doubly charged for non-sequential double ionization as a function of ellipticity at 800nm, 40fs and $1.2 \times 10^{14} W/cm^2$.

The plot shows the ionization yields of doubly charged argon as a function of ellipticity, where maximum re-collision occurs at linear polarization then it falls off rapidly. However, the case is different for chiral molecules depending on the type of the molecule. It is found that the ellipticity value corresponding to maximum signal is not exactly zero but shifted slightly. This shift was different depending on the handedness of the chiral molecule.

Chapter 2

Experimental Method

The experimental setup will be described in details in this Chapter, including a description of femtosecond laser system which was used to perform the experiments and time-of-flight (TOF) system where the molecules are ionized and the ions are detected.

2.1 Femtosecond Laser System

The photoionization experiments were conducted using amplified Ti:Sapphire laser system from Spectra-Physics. This system consists of a femtosecond oscillator (Tsunami, Spectra-Physics, Santa Clara (USA)) pumped by a 5W $Nd:YVO_4$ diode solid-state laser (Millenia, Spectra-Physics, 532 nm). The oscillator generates pulses that have a pulse duration of 20 fs, pulse energy of 8nJ operating at a wavelength of 800 nm and repetition rate of 76 mHz. Pulses from the oscillator are amplified by a regenerative amplifier (Spitfire pro, Spectra-

Physics) pumped by a 30W laser. The chirped pulse amplification (CPA) technique is used to avoid damaging the optics during the amplification process. This technique permits the Ti:Sapphire crystal to maintain the power density inside the amplifier below the damage threshold in order to amplify the pulses beyond its damage threshold. The amplification process consist of three steps: i) the short seed pulse coming from a stable mode-locked femtosecond laser are stretched by a large amount in order to reduce its peak power. So the intensity is reduced by (10^6) when the duration is increased by (10^6). A multi-pass grating is used to stretch the pulses. The grating allows the low-frequency components to travel shorter path, unlike the high-frequency components. After passing through multi-pass grating, the pulse is positively chirped and has a longer pulse duration. ii) The stretched pulses, which have a lower intensity than the damage threshold, are amplified by passing through the regenerative amplifier several times. The pump laser gives a coherent energy pulse to the Ti:Sapphire crystal in order to excite it to a high energy state before the stretched pulses' arrival. Stimulated emission is obtained and the pulses are amplified at the same wavelength. iii) Finally, the amplified pulses are recompressed by a grating compressor. The repetition rate is reduced to 1 kHz producing $40fs$ pulses with an output power of $2.5W$.

The pulse duration was measured using an autocorrelation technique. It was important during the experiment to monitor the pulse duration to make sure that it was kept as low as possible. Laser pulse energy and duration are important parameters to determine intensity used in photoionization. From the measured pulse energy E_p, the peak power is obtained from

$$\mathbf{P_p} = \mathbf{f_s}\frac{\mathbf{E_p}}{\tau_\mathbf{p}} \tag{2.1}$$

where f_s is a numerical factor which is a function of pulse shape (0.94 for a Gaussian distribution, and τ_p is the pulse duration.

The experiments in this thesis were carried out at $2000nm$ wavelength as well as $800nm$. The $40fs$ generated pulses at $800nm$ wavelength by the Ti:Sapphire laser were sent to an optical parametric amplifier (OPA) producing pulses in the mid-infrared region. The OPA pumped at a frequency w_p, produces signal and idler at frequencies w_s and w_i respectively, where $w_p = w_s + w_i$. In the presence of a weak signal beam at the nonlinear crystal, the pump beam is depleted, the signal beam is amplified and third beam, which is the idler is generated. The output beam (the signal or idler) is spatially filtered and then amplified by a BBO crystal.

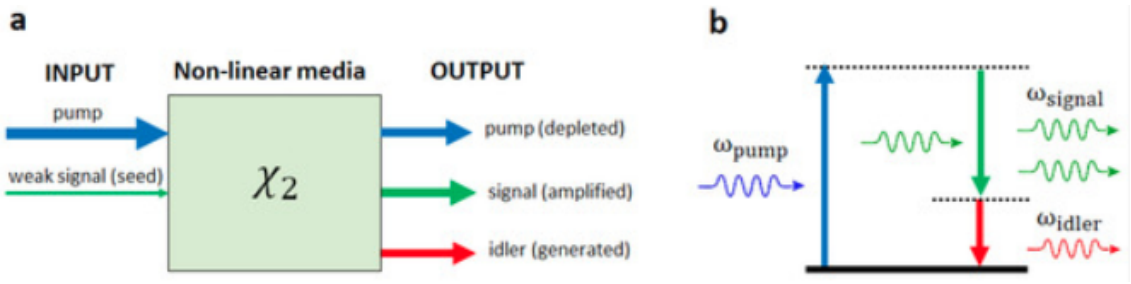

Figure 2.1: a) Power flow from the pump beam to the signal beam in optical parametric amplification; (b) the same optical parametric amplification process can be viewed as stimulated emission of signal photons from a virtual level excited by the pump. Picture and caption are reproduced with permission from [34].

The polarization dependence of elliptical light polarization is increased at $2000nm$ due to the long time duration that the electron propagates in the laser field. The electron wavepacket is highly affected by the laser field as it spends more time in it. Doing the experiments at different wavelengths allows us to compare the results, therefore, provide

an opportunity to interpret the results that are related to chiral molecules. Also, at long wavelength the role of B-field becomes significant [35]. Strong field ionization is typically treated within the dipole approximation which ignores the magnetic effects because of its small contribution to the Lorentz force. As a result, the trajectory of the electron is always in the polarization plane. However, when including the magnetic field, high-energy electrons are affected by the magnetic field, since the Lorentz force acting on the electrons depends linearly on the ratio v/c (v is the electron velocity and c is the speed of light). These high-energy electrons in strong-field ionization results from intense-long waverlength. Consequently, the magnetic field exert a force on the ionized electron which no longer oscillates in the plane of the polarization.

2.2 TOF Mass Spectrometer

The mass spectrum of chiral molecules were obtained using a Wiley-Mclaren time of flight mass spectrometer. The Wiley-Mclaren system is based on a two-grid, double field source with repeller and extractor dimensions optimized for resolution [36]. A time-of-flight mass spectrometer (TOFMS) consists of three essential parts: the extraction region, field free drift tube and the detector. TOFMS functions as follows i) the ions start in the ionization region, ii) under the influence of E-field, the ions are extracted and accelerated from the ionization region passing through a 1mm x 9mm slit in the middle of the extractor plate to field free drift tube. The E-field is generated via a repeller and extractor of $2000nm\ V/m$ and $1000V/m$ respectively in order to extract the ions from the ionization region to the field free

drift tube. Finally, the ions are detected by a microchannel plate (MCP) placed at the end of the TOF. The TOF apparatus is sketched in Fig.2.2. The MCP detects charged particles through generation of secondary electrons. These electrons are detected by anode and after preamplification are sent to a constant fraction discriminator (CFD) to remove timing jitter so the arrival time for a specific m/q is accurately determined.

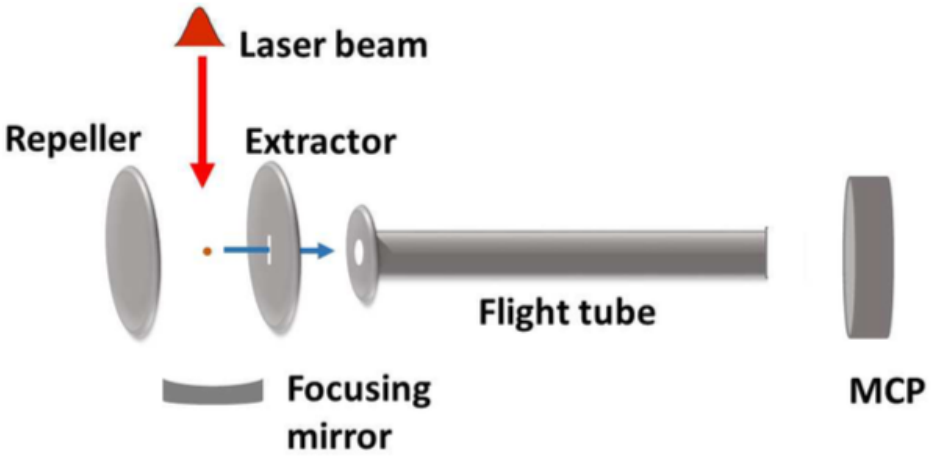

Figure 2.2: Schematic of the time-of-flight mass spectrometer. Image is reproduced from [28].

Since the anode signal is a sharp pulse, finding the peak is difficult resulting in timing jitter. CFD reduces this by duplicating the pulse, inverting it and joining it again a short delay. The zero crossing point now allows to actually determine the arrival time of the ion on the detector. A time-to-digital convertor is used to record the arrival time of various ions.

The time that the ion needs to travel from the extractor to the MCP detector is given by [37]:

$$\mathbf{t = L\sqrt{\frac{m}{(2zeV)}}} \tag{2.2}$$

Where L is the tube length, V is the interaction voltage, m/z is the mass to charge ratio, e is the electron charge.

2.2.1 Data Capture

The MCP sends the detected ion signal to a multi-channel digitizer (time to digital converter). A computer software captures the total ion counts per specific time and then generates a spectrum. The software displays the time delay on the x-axis and the ion count on the y-axis. Then, the spectrum is calibrated for m/q by identifying the H_2O, O_2 and N_2 peaks visually. These peaks exist in the chamber even at the extreme vacuum level. Intensity calibration can be verified by comparing the values of the ionization saturation for molecules (such as Ar or Xe) with known value from the literature (more details provided in section (2.7)).

2.3 Vacuum System

The vacuum system consists of two chambers connected by a small tube in order to achieve differential pumping. The pumping speed decreases with the cross section and we have one chamber with high vacuum and the other has low vacuum. Achieving differential pumping is critical because the detector has to be in a high vacuum (10^{-6} Torr) if not we will have a lot of background counts, and then the detector will be damaged as shown in Fig2.3. The high

vacuum is obtained by using turbo pump backed by rough pump. The rough pump is used to bring the pressure down to 10^{-3} Torr and then the turbo pump is used to bring the pressure down to 10^{-9} Torr. To obtain the required pressure, it is necessary to pump the vacuum 48 hours before conducting the experiment. Once the vacuum pressure has been achieved and all settings are stable, it is important to monitor the pumps' current regularly to ensure effective operation throughout the experiment. Since the sample is in a liquid phase, a test tube is connected to a directional flow control manifold built from copper pipe and valves to allow the chiral molecular to enter the vacuum system. Limonene has low vapor pressure, so the sample has to be heated to introduce the sample into the vacuum chamber in the gas phase. The gas enteres the chamber through a flexible teflon hose. It is critical to pump down the hose, valves and fittings before introducing new chemicals because these parts contain residual traces of chemicals, from previous experiments. A separate rough pump is connected via the control manifold to enable this and a pressure sensing gauge is attached to ensure that the correct gas pressure is attained before shutting the valve leading to the test tube source. From there, two additional valves lead to the entrance of the chamber that are sequentially opened to ensure slow and accurate pressure build up in the chamber.

The spectrometer has a FWHM mass resolution of 550 for a range of $0 - 137$ m/z. We have approximately 50 counts precision over the course of the observation period which is 1 minute; equating to 60 000 samples. This provides approximately a 0.1 percent error tolerance. The data is acquired using 100,000 laser shots and pulse duration of $40 - 110fs$. In addition to that, the system noise and counting error can prevent a precise measurement

and differentiation between molecules and their fragment. Thus, it is very important for the experiment to prevent the chamber contamination to discriminate the desired molecules, and this can be done at the chamber background vacuum levels in 10^{-9} Torr.

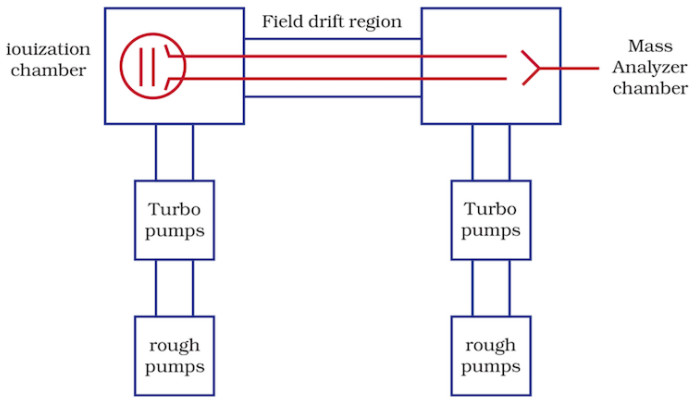

Figure 2.3: Vacuum system for mass spectrometry.

2.4 Optical Setup

To obtain effective ionization, it is critical to have precise alignment from the laser to the chamber. It is important to ensure the alignment accuracy before doing the measurement to gain precise and accurate measurement. The laser beams traverses three optical tables before reaching the experimental setup. Since we have the laser beam passing through a long distance from the laser source to the chamber, irises are placed and aligned in the path of the beam from the laser source to the chamber to ensure that the beam is aligned parallel to the benches and to make any adjustment needed before moving any further. The laser pulses which are generated from the amplification source pass through a beam splitter. This beam splitter is used to reflect a small part of the beam into the autocorrelator to measure

the pulse duration, the rest of the beam will pass through. The set up is illustrated in Fig. 2.4.

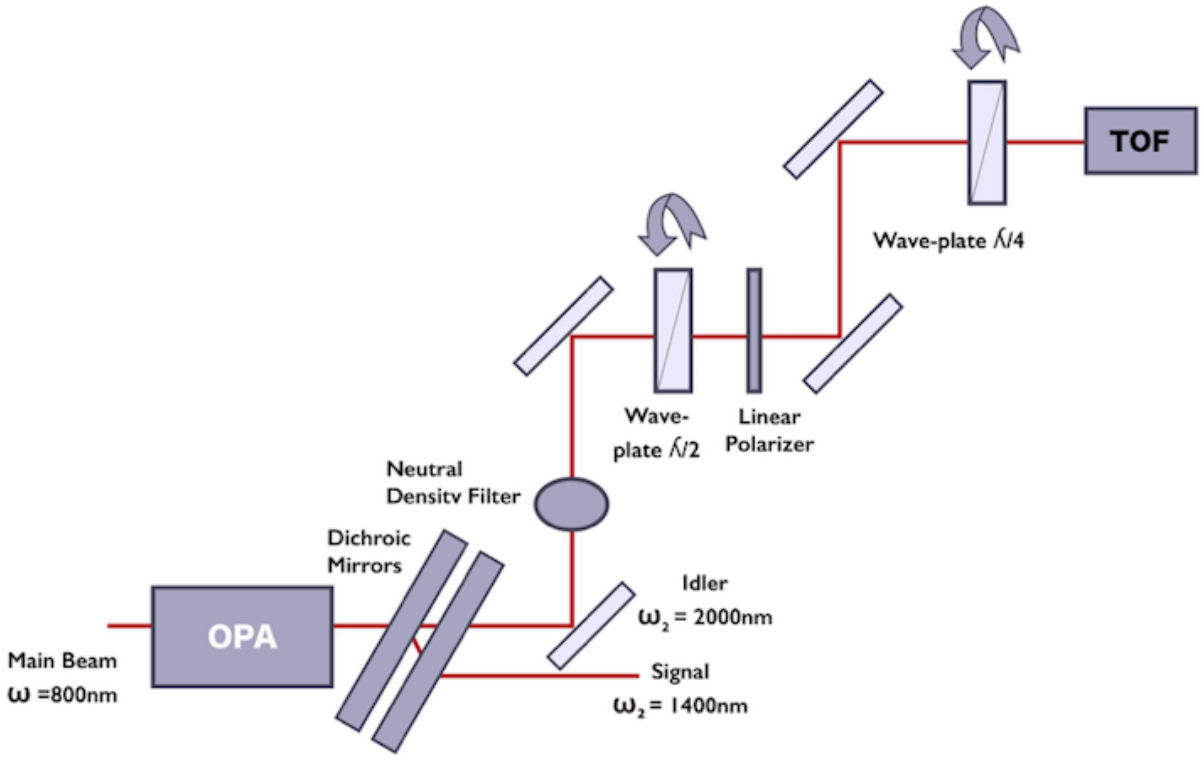

Figure 2.4: Experimental setup of optics.

The laser beam passes through a combination of half wave plate then a polarizer in order to control the laser power. Then, it passes through a quarter wave plate for polarization control to the chamber‘s window. The laser pulses passes through a fused silica window, then to a focusing mirror inside the chamber to focus at the center of the interaction region of TOF. Via the gas manifold, molecules under study are leaked into the vacuum system. Upon ionization at the center of the TOF the ions are accelerated and detected by the MCP. It is also important to align the mirror inside the chamber in order to obtain maximum focusing

of the laser beam. The mirror was mounted on a three dimensional translation XYZ to control the focus and allowing any adjustment should be made in all planes. Before the final alignment of internal mirror, it is necessary to open the chamber and align the beam directly to the center of the two plates (repeller and extractor) therefore the center of the focusing mirror. The alignment of the focusing mirror positioned for the maximum signal. Finally, checking the back reflection to be very close to the main beam is very crucial in order to ensure precise alignment.

2.5 Pulse Energy Control

It is important to vary the pulse energy and the polarization of the laser beam to assess the response on the ionization dynamics. Accurate measurement is very important in order to determine the amount of energy entering the chamber and to keep the energy levels under saturation or damage threshold levels. To control and measure the pulse energy, a combination of half wave plate and polarizer are used in the setup. This combination will provide linear and consistent graduation in energy as well as precise measurement. The HWP rotates the polarization plane of the incoming beam by 2 (θ). As a result, when the polarization direction of the linearly polarized light is rotated, only the E-field vector which is aligned with the polarizer can be transmitted.

2.5.1 Polarization Control

A quarter wave plate (QWP) on a motorized rotation stage was used to convert the polarization from linear to circular. In order to calibrate the QWP to obtain the desired polarization, the maximum energy E_{max} and minimum energy E_{min} of the beam was measured via a polarizer for a given position of the QWP. The maximum value of the (E_{min}/E_{max}) ratio gives us circular polarized light. Whereas, at the minimum value of (E_{min}/E_{max}), we obtain linear polarization. Elliptically polarized light can be obtained at the values between $0 - (\pm 1)$ of (E_{min}/E_{max}) ratio. Theoretically, the maximum ratio $(E_{min}/E_{max} = 1)$ corresponds to circularly polarized light and the minimum value $(E_{min}/E_{max} = 0)$ corresponds to linearly polarized light. However, we cannot achieve the exact value practically. For example, we obtained $\epsilon = 0$ for linearly polarized light and $\epsilon = 0.98 \simeq 1$ was obtianed for circularly polarized light.

2.6 Mass Calibration

It is difficult to identify TOF peaks when working with large molecules. The complexity of ionized molecules spectrum makes it difficult to discern accurately when using mass to charge ratio only. Therefore, it is very important to discriminate the peaks properly by calibrating the molecular mass from TOF values to the expected amu values. Given that precise beam alignment in the x,y and z-axes are normally adjusted at the time of experiment to maximize ion yield, the precise distance from the TOF ionization point to the MCP detector varies and must therefore be compensated in the conversion of flight time to m/z. Atoms, such as xenon

are used for calibration because it has large number of isotopes so both singly and multiply charged ions can be used to accurately calibrate mass spectrum. Also, the isotopomer ratio of Xe is known. So, one can compare them to ensure you are not operating in saturation regime Fig.2.5. After the mass calibration, the molecular spectrum which is under study can be identified when it is compared to a reliable reference.

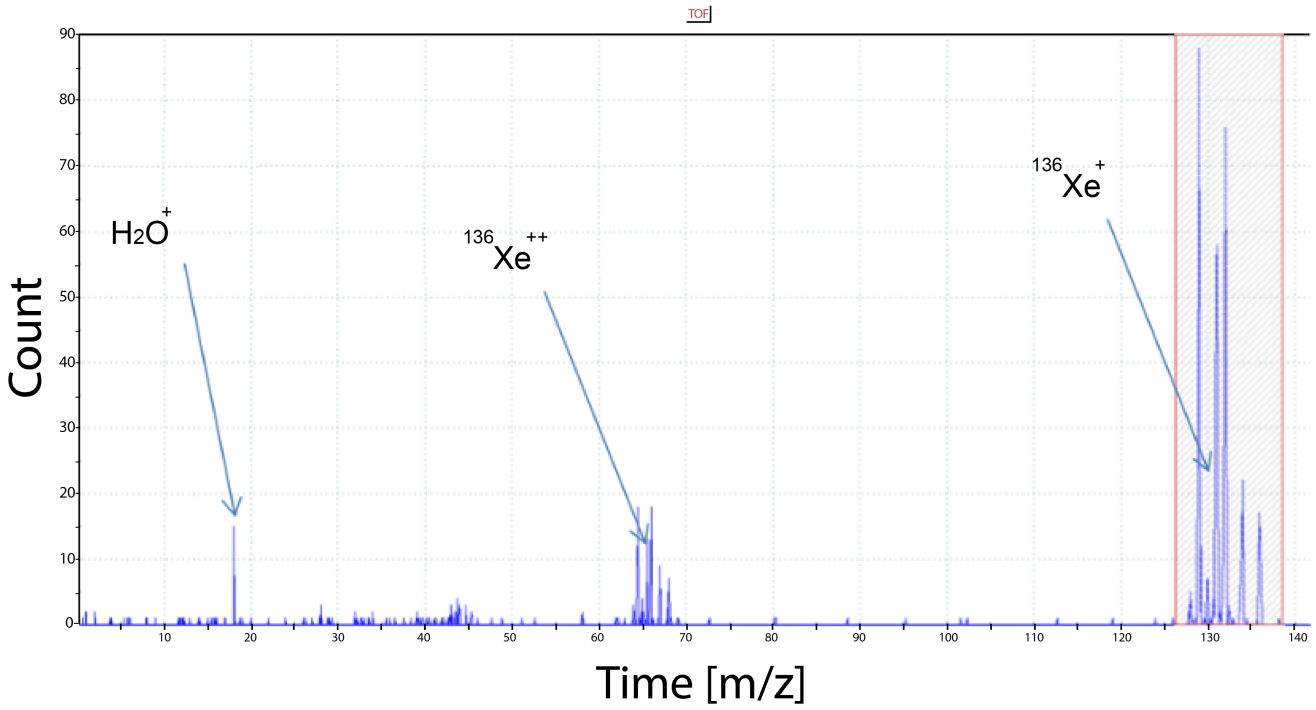

Figure 2.5: Mass spectra for Xe taken at $15\mu J$, $4.2 \times 10^{-8} Torr$ shows the presence of singly and doubly charged ions.

For atoms and molecules, the relative abundance of the respective isotope ions to parent ions on the TOF mass spectrum permits us to discriminate directly the parent ions of interest since the relative abundances are known from reference which is explained in chapter 3.

2.7 Intensity Calibration

Since all nonlinear matter interactions depend on the intensity, we need to accurately know the intensity at which the ionization results are obtained. For example, the freed electron energy which is obtained during the acceleration in the laser field depends on the intensity. Intensity can be obtained directly by measuring the spot size since $I = \frac{Energy}{time \times area}$. However, measuring the spot size is tiresome becuase it can not be measured directly on a day-to-day basis. alternatively, we measure the saturation intensity of an atom by measuring the ionization signal count of an atom such as argon or xenon. The saturation intensity is defined as the intensity at where 43% of the target is ionized [38]. The ion yield count is plotted as a function of the laser pulse energy in a semi-log plot 2.6. Atoms are ionized completly in the most intens part of the when reaching higher pulse energies. The linear portion of the ion signal curve provides the asymptotic ionization rate behavior resulting from the expansion of the focal volume as the pulse energy increases. Extrapolating this portion back to the horizontal axis gives the pulse energy which saturate the target. The intersection of the X-axis of the curve below is the saturation energy E_{sat} [39]. By comparing the saturation energy which we get from the experiment to a known value from the literature, we can get the saturation intensity. The measurments are taken below the saturation intensity because taking the measurments above the saturation intensity will alter the maximum ellipticity.

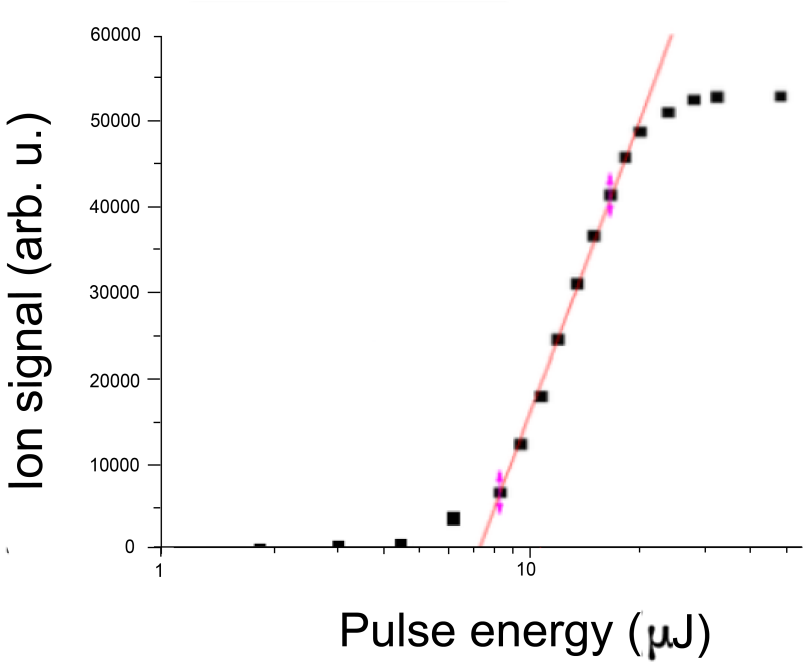

Figure 2.6: A semi-log plot of Xenon yield as a function of pulse energy at 800 nm, 4.4×10^{-8} Torr.

We can also observe the saturation from the mass spectrum, it provides a visual indication of saturation. Fig2.7 shows the mass spectrum of Furan and varying intensities. The distortions at the side of the parent ion peak indicates saturation because there are too many ions per laser shot (which means for every start signal there are too many stop signals) the electronics can not handle it. Therefore, instead of recording the stop signal to be at X ns, it spills over into the next few time bins leading to distortion in the peak shape.

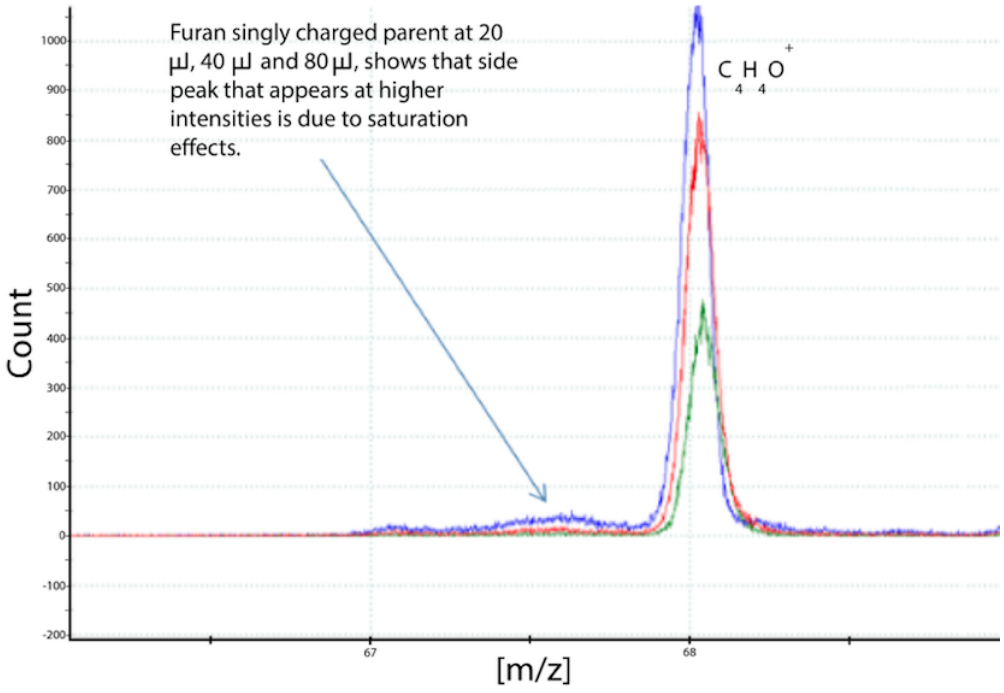

Figure 2.7: Qualitative saturation observations provide a visual indication of saturation as singly charged ions are no longer ionized proportionately in the focal volume. Image is reproduced from [27].

Chapter 3

Chiral Molecule Photoionization

3.1 Mass Spectrum of Limonene

The relative isotopic abundance in the TOF mass spectrum allows us to identify and confirm the doubly charged molecular ions. Limonene parent ion $(C_{10}H_{16})^{+}$ is at $m/z = 136$ and its isotopomer $(^{13}C^{12}C_9H_{16})^{+}$ is at $m/z = 137$. The doubly charged ion $(C_{10}H_{16})^{++}$ overlaps with the fragment $(C_5H_8)^{+}$ at $m/z = 68$. The doubly charged and the fragment can be distinguished using the parent ion isotopomer $(^{13}C^{12}C_9H_{16})^{+}$. The doubly charged isotopomer $(^{13}C^{12}C_9H_{16})^{++}$ at $m/z = 68.5$ Fig3.1. Any signature of doubly charged can be made by looking at isotopomer ratio. Limonene will have isotopes at 135, 137 and 138. So if there is a peak at 68.5 or 67.5 then that means there is contribution of doubly charged to the peak at 68. Moreover, when the ellipticity is varied, any residual signal at circular polarization is an indication of the amount of fragment because non-sequential double ionization should

vanish for circular polarization.

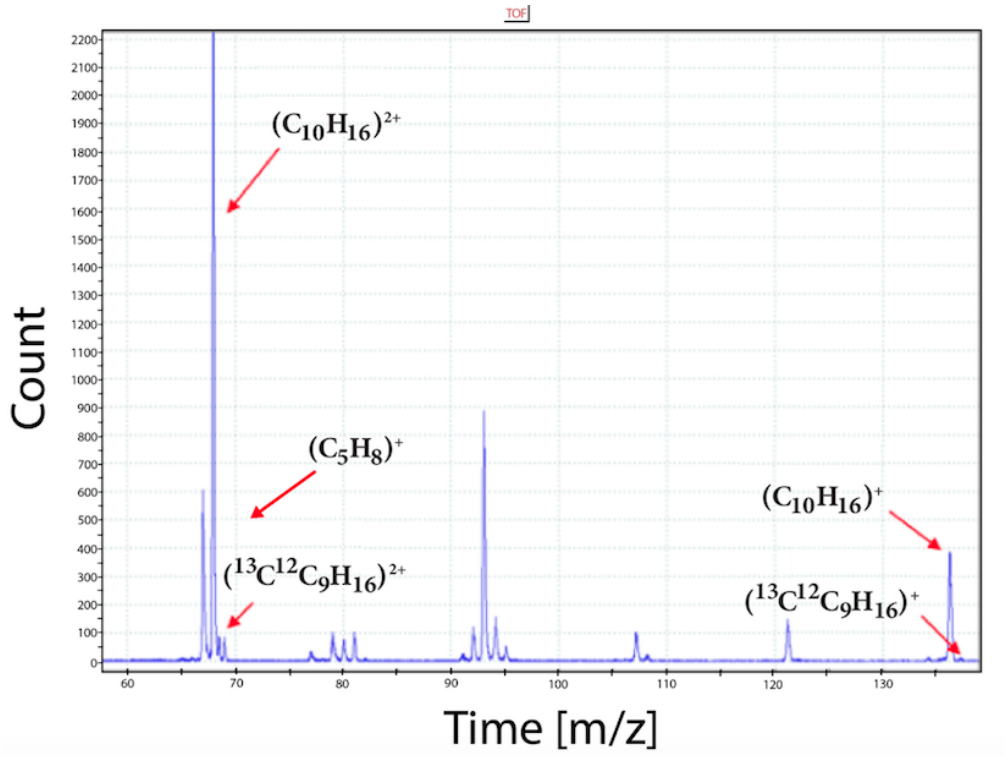

Figure 3.1: Mass spectra of limonene shows the presence of singly and doubly charged ions together with their isotopes. The spectrum was taken at 800 nm with intensity1.1×10^{14} W/cm^2, 2×10^{-6} Torr, ellipticity $\epsilon = 0$.

3.2 Ellipticity Variation in Chiral Molecule

3.2.1 Limonene, 800nm

The result presented here is for (R)-limonene and (S)-limonene. The measurements were taken from -45 to +45 QWP angle producing -1 to 1 ellipticity change. The ionization counts were obtained at $1.1 \times 10^{14} W/cm^2$. This low intensity was chosen to minimize saturation

effects.

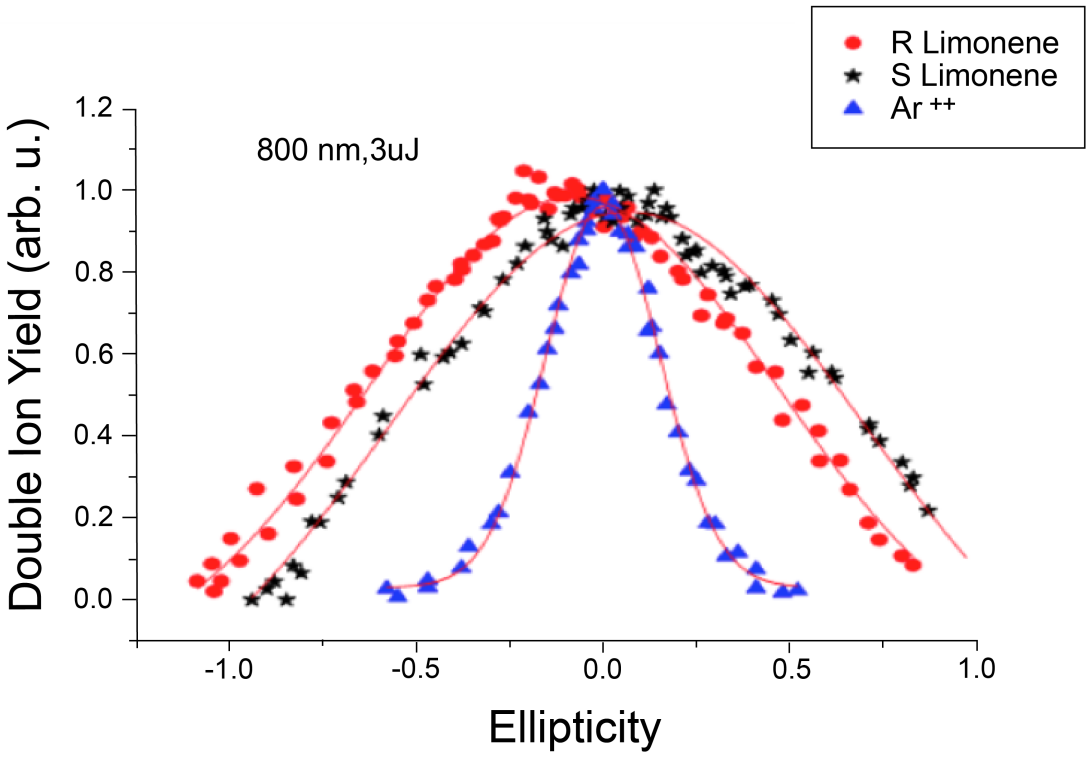

Figure 3.2: Ellipticity result of double ionization, $800nm$ at $1.1 \times 10^{14} W/cm^2$.

The blue triangles are Argon and the red circles and black stars are (R) and (S) limonene respectively. For argon the maximum counts are at zero ellipticity but for (S) and (R) limonene, the maximum is shifted on either side. One is to the left of argon and the other to the right. This shift allows us to distinguish the two enantiomers.

For a better understanding, we took the ratio of (S) and (R) limonene of doubly and singly charged Fig3.3. We see here there is a difference in the doubly charged (Red). However, there is no difference in the singly charged (Blue) for the two enantiomers. In the middle region, there is a less signal noise because of the high signal count.

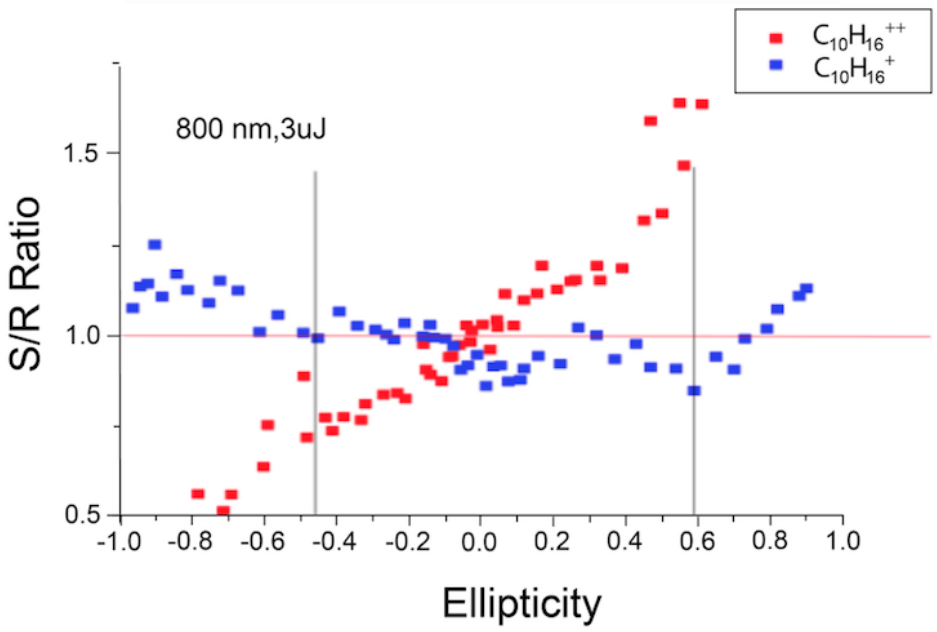

Figure 3.3: Ratio of (S)/(R) limonene using $800nm$ at $1.1 \times 10^{14} W/cm^2$ (blue square represents limonene singly charged ion) and (red square represents doubly charged ion of limonene).

3.2.2 Limonene, $2000nm$

The measurements were done with $2000nm$ at $1.1 \times 10^{14} W/cm^2$. Fig3.4 shows a difference in the doubly charged as well. Surprisingly, when the ratio of (S) and (R) limonene of singly and doubly charged were taken Fig3.6, it appears that there is a difference in the singly charged too. So, at longer wavelength, a difference arises between (R) and (S) limonene in doubly charged as well as singly charged.

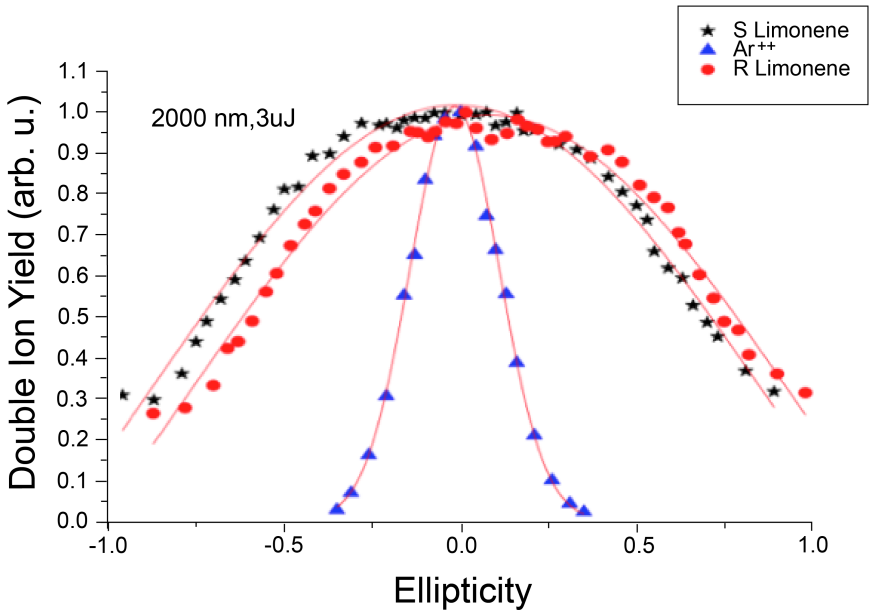

Figure 3.4: Ellipticity result of double ionization, $2000nm$ at $1.1 \times 10^{14} W/cm^2$.

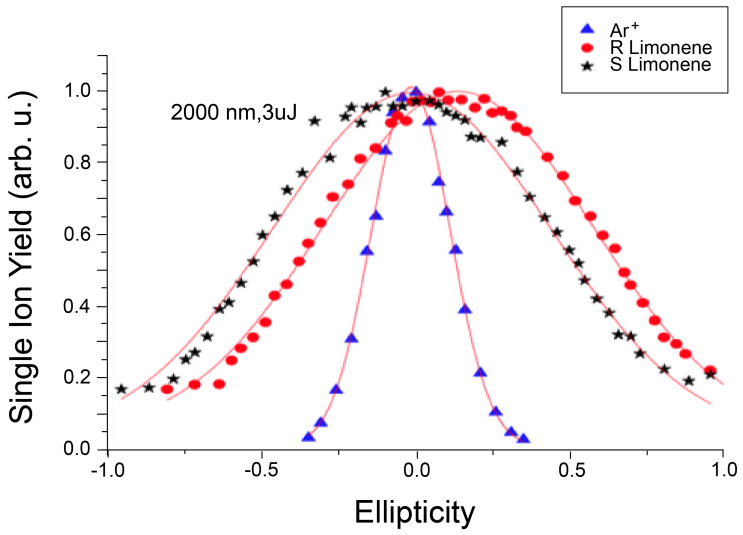

Figure 3.5: Ellipticity result of limonene single ionization, $2000nm$ at $1.1 \times 10^{14} W/cm^2$.

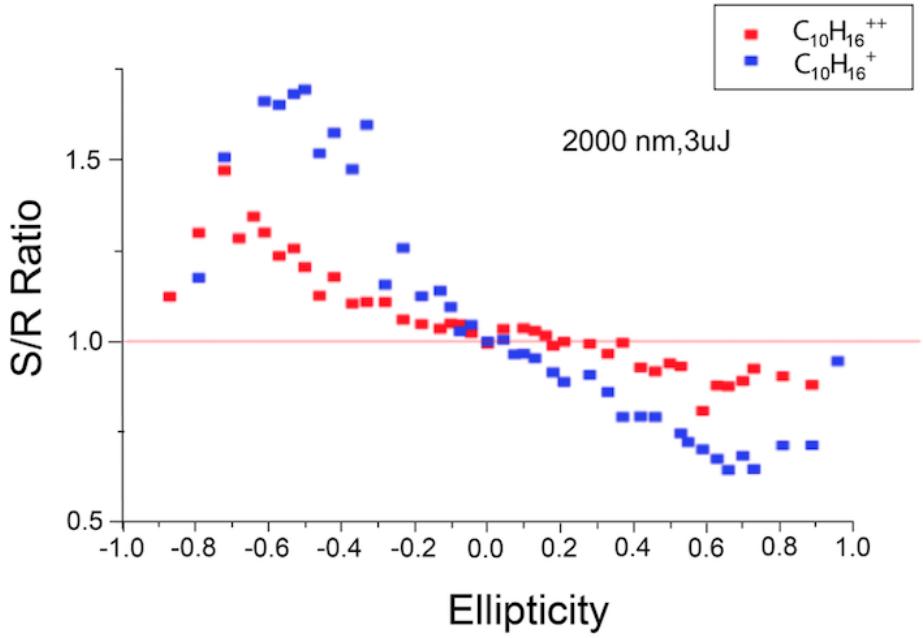

Figure 3.6: Ratio of (S)/(R) limonene using $2000nm$ at $1.1 \times 10^{14} W/cm^2$ (blue square represents limonene singly charged ion) and (red square represents doubly charged ion of limonene).

3.2.3 Camphor,$(C_{10}H_{16}O)$, $2000nm$

The measurments were carried out using a different chiral molecule, which is camphor $(C_{10}H_{16}O)$. Camphor ionization potential is 8.76 eV and the molecular structure is depicted in Fig3.7.

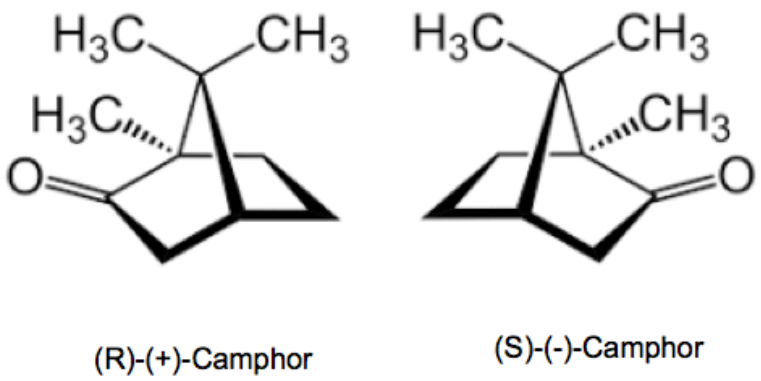

Figure 3.7: Camphor molecular structure.

The results were conducted at 2000nm as well at $1.1 \times 10^{14} W/cm^2$. No difference could be observed between left handed and right handed camphor in the fragment $C_6H_9^+$ as shown in Fig3.8 (the result was obtained using fragment because there was no doubly charged peak). By taking the ratio of (S) and (R) camphor of singly charged and the fragment, we can see that there are no differences Fig3.9.

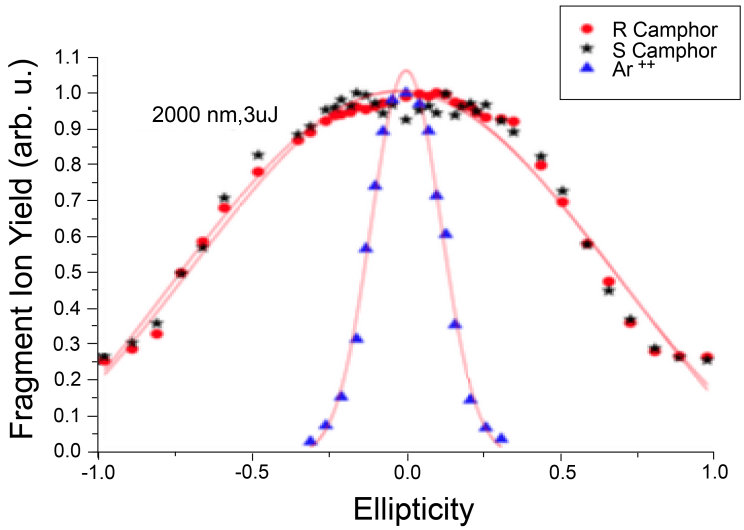

Figure 3.8: Ellipticity result of fragment yield, $2000nm$ at $1.1 \times 10^{14} W/cm^2$. (The blue triangles are argon and the red circles and black stars are (R) and (S) camphor respectively).

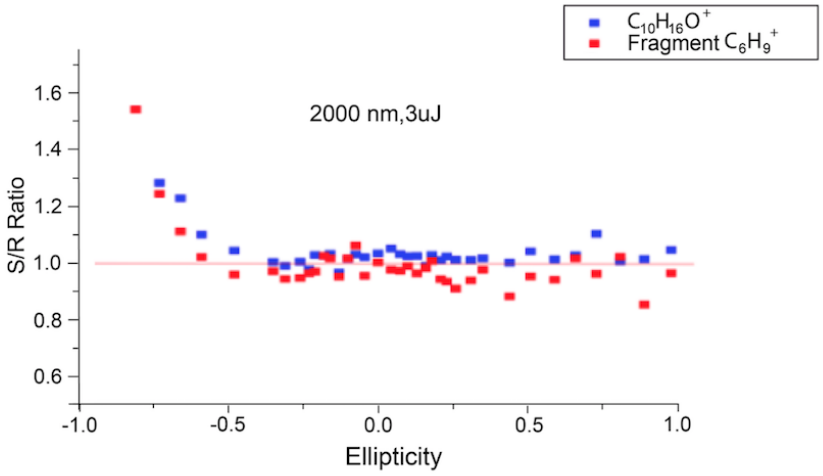

Figure 3.9: Ratio of (S)/(R) camphor using $800nm$ at $1.1 \times 10^{14} W/cm^2$ (blue square represents camphor singly charged ion) and (red square represents the fragment $C_6H_9^+$ of camphor).

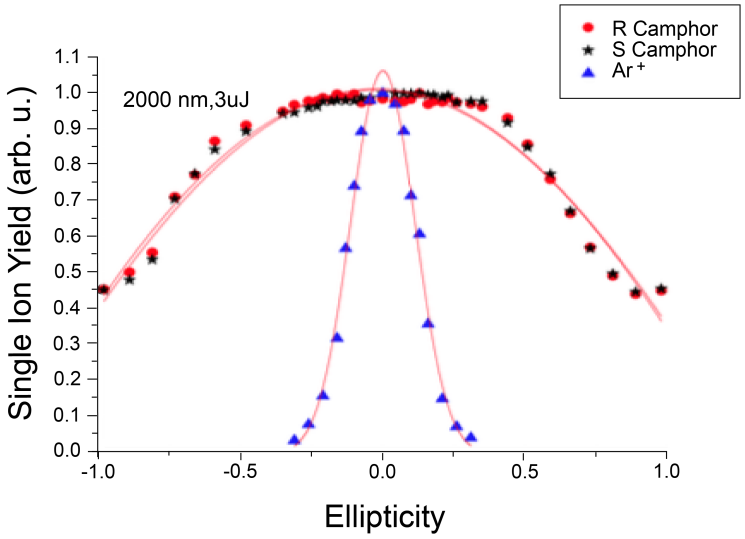

Figure 3.10: Ellipticity result of single ionization, $2000nm$ at $1.1 \times 10^{14} W/cm^2$.The blue triangles are argon and the red circles and black stars are (R) and (S) camphor respectively.

3.2.4 Fenchone $(C_{10}H_{16}O)$, $800nm$

Fenchone ionization potenatial is $8.5eV$ and the molecular structure is shown in Fig3.11

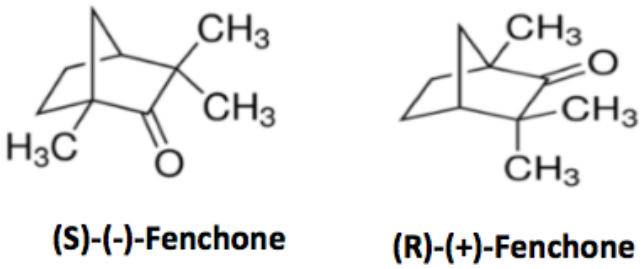

Figure 3.11: Fenchone's molecular structure.

The results were conducted at $800nm$ at $1.1 \times 10^{14} W/cm^2$. The finding was that no difference between left handed and right handed fenchone in the fragment nor the singly charged. By taking the ratio of (S) and (R) fenchone of the fragment and singly charged Fig3.12, we can see that there are no differences. Also with fenchone, no doubly charged peak appears in the spectrum, so the result was carried out using the fragment peak.

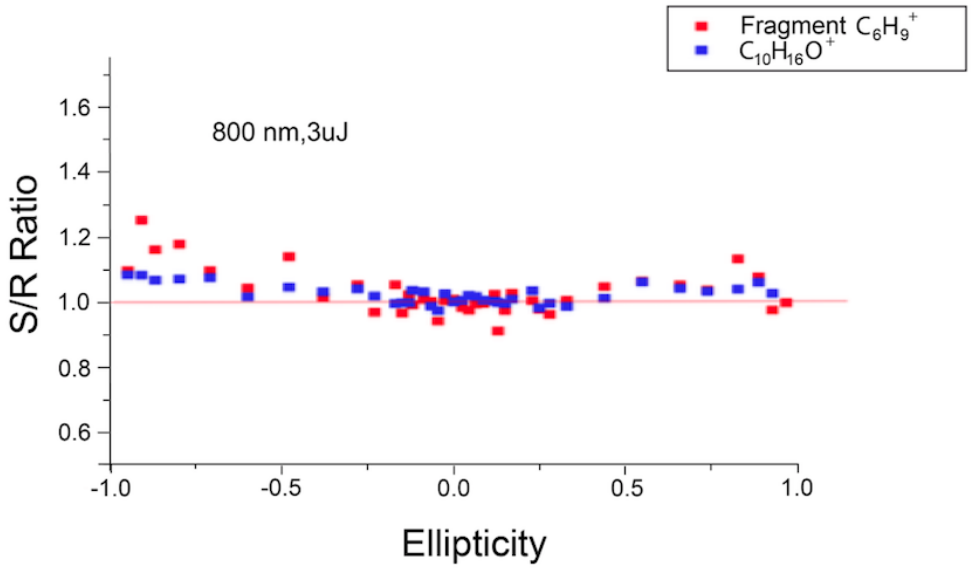

Figure 3.12: Ratio of (S)/(R) fenchone using $800nm$ at $1.1 \times 10^{14} W/cm^2$ (blue square represents fenchone singly charged ion) and (red square represents fragment $C_6H_9^+$ of fenchone).

Also, the same result is obtained for (R) and (S) fenchone at 2000nm Fig3.13.

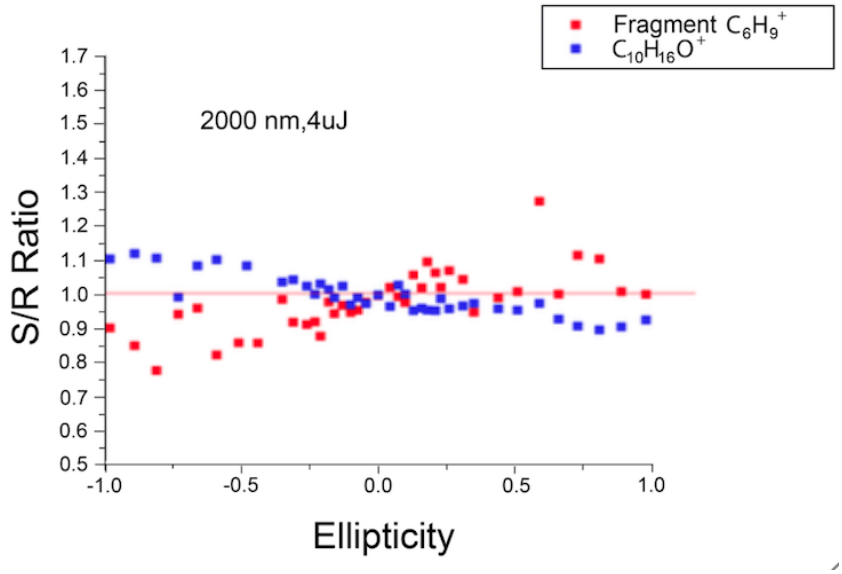

Figure 3.13: Ratio of (S)/(R) fenchone using $2000nm$ at $1.1 \times 10^{14} W/cm^2$ (blue square represents fenchone singly charged ion) and (red square represents fragment $C_6H_9^+$ of fenchone).

3.2.5 Propylene Oxide, C_3H_6O, $800nm$

Ionization potential of propylene oxide is $10.1eV$ and the molecular structure is shown in Fig3.14

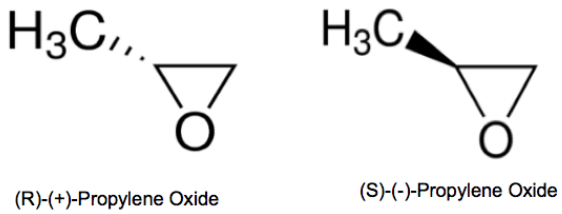

Figure 3.14: Propylene oxide molecular structure.

The results were conducted at 800nm at $1.1 \times 10^{14} W/cm^2$. No difference arises between left and right handed propylene oxide in the doubly and singly charged. When the ratio of (S) and (R) propylene oxide of singly and doubly charged ions were taken, no difference is observed, see Fig3.15.

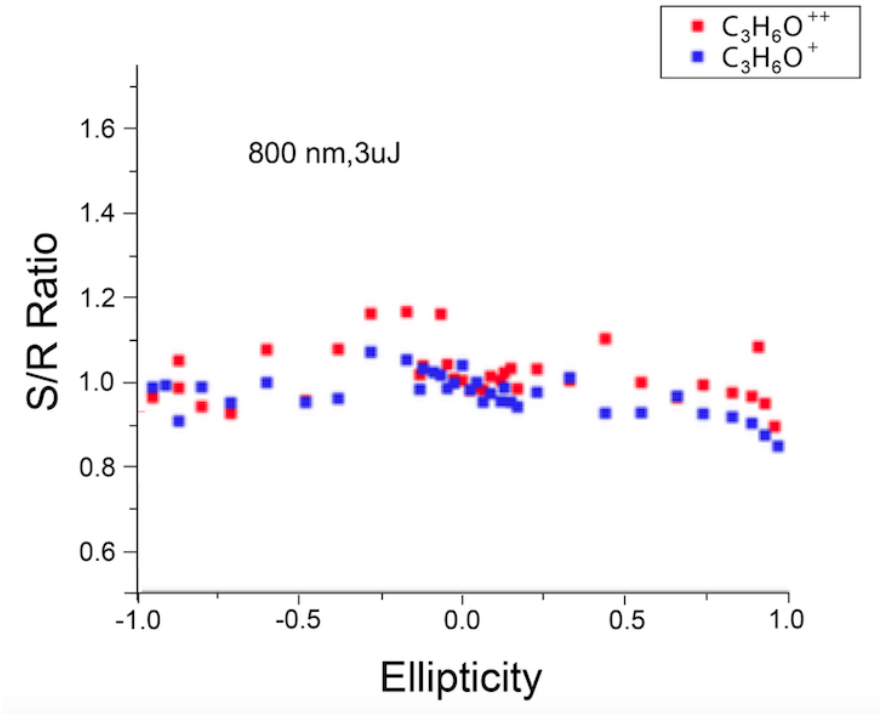

Figure 3.15: Ratio of (S)/(R) propylene oxide using $800nm$ at $1.1 \times 10^{14} W/cm^2$ (blue square represents propylene oxide singly charged ion) and (red square represents doubly charged ion of propylene oxide).

3.3 Discussion

Recollision is often described within the dipole approximation, which means that the magnetic field is neglected. In dipole approximation, if the plane of polarization is chosen as

reflection plane then (R) molecules gives (S) molecules upon reflection. However, the electric field remains the same on this reflection. So, within dipole approximation recollision is the same for enantiomers. On the other hand, in non-dipole approximation, the magnetic field has different impacts on the molecules. These impacts become important whenever the motion of the electron in the field is greater than a Bohr radius, which could take place at a longer wavelength and high intensities [40]. When including the magnetic field, there are three possibile mechanisms:

i) As the ionized electron propagates in the laser field, the laser field induces magnetic dipole transitions in the ion exiting it. As the electron returns, it recollides with excited ion. So, the recollision takes place with an exited ion.

ii) Inelastic collision between the recolliding electron and the parent ion which leads to promoting the cation to high excited state. Elliptical polarized laser field induces electric and magnetic dipole transitions in the high excited state, hence, chiral response arises.

iii) The laser magnetic field acts on the freed electron. The Lorentz force causes the electron trajectory to be out of the plane. By using elliptically polarized light, the electron's trajectory becomes chiral. Chiral signal can arise when, (a) the recolliding electron undergoes scattering from the chiral center differently. or (b) The magnetic field and recollision together can act as a gate. The ellipticity gate leads to asymmetry in the transverse momentum of the ionized electron and hence the double ionization [41].

Nevertheless, can we generalize this result on all chiral molecules? Is this result universal? The experiments were done on another three chiral molecules: camphor, fenchone

and propylene oxide.

We can see that there are differences in limonene but not camphor, fenchone, and propylene oxide. So, the Lorentz force is a universal mechanism and it should be present in all molecules. But, this mechanism is less likely to play a role because it relies on the electron trajectory, whereas, the type (i) and (iii) relies on the field induced magnetic transitions from intermediate state. In this case, the magnetic dipole transitions that are being induced in the ion seems to be different for limonene and the other three chiral molecules. Also, we see a difference in singly charged of limonene, which means that there could be the magnetic dipole transition that is hitting the resonance in limonene but not in camphor, fenchone and propylene oxide.

In summary, more theoretical calculations need to be carried out in order to isolate and identify the mechanism.

.

Chapter 4

Conclusion

The experiments were carried out using chiral molecules, namely limonene ($C_{10}H_{16}$), camphor($C_{10}H_{16}O$), propylene oxide (C_3H_6O) and fenchone ($C_{10}H_{16}O$). Chiral molecules have important implication in biology, biochemistry and pharmaceutics.

Despite all the techniques that have been used to study chiral molecules such as circular dichroism, photoelectron circular dichroism, Coulomb explosion, etc, all these techniques have their limitations. Therefore, we used photoionization via mass spectrometry to detect chirality using elliptically polarized light. We have demonstrated that photoionization using elliptically polarized light can discriminate left and right handed molecules. However, this method is not valid for all molecules as explained earlier. Also, we can see differences in singly charged as well as doubly charged ions at longer wavelength. These differences arise in non-dipole approximation where the magnetic field becomes important and that occurs when the electron motion is larger than a Bohr radius. In the non-dipole approximation, two

mechanisms would play a role:

i) The Lorentz force pushing the electron out of the polarization plane, which leads to chiral discrimination when the electron recombines with the parent ion and ellipticity gating with magnetic field acting together.

ii) Magnetic dipole transition in the ion carrying it while the electron is propagating and returning to the ion. In other words, the recollision takes place in a magnetically mediated excited state just like in HHG.

So far, we believe that there is still much to be understood about this mechanism. In addition, this result raises some opportunities to develop theoretical insights to understand the molecular dynamics. In the future, experiments will be focused on using orbital angular momentum (OAM) beams to study ionization dynamics. Left and right circular polarization with OAM leads to two types of chirality; one is due to circular polarization and the other is due to the OAM beam. In addition, future work will be expanded to look at linear and nonlinear absorption by using left and right OAM beam in a chiral system.

Bibliography

[1] D.G. Blackmond. The origin of biological homochirality. *Cold Spring Harbor Perspectives in Biology*, 2(5):pp. 2878–2884, p.a002147, 2010.

[2] V. Schurig and F. Balzano. *Differentiation of Enantiomers II*, volume 341. Cham: Springer, 2013.

[3] H. Utsuno and T. Asami. Maternal inheritance of racemism in the terrestrial snail bradybaena similaris. *Journal of Heredity*, 101(1):11–19, 2009.

[4] P. Jordan and R.de.L Kronig. Movements of the lower jaw of cattle during mastication. *Nature*, 120(3031):807, 1927.

[5] E. Siegel. Is our universe left-handed? (synopsis). *Science Blogs*, July 25 2014, [Online]. Available: view-source:https://scienceblogs.com/startswithabang/2014/07/24/is-our-universe-left-handed-synopsis. [Accessed 18 06 2020].

[6] G.H. Wagnière. *On chirality and the universal asymmetry: reflections on image and mirror image*. Zürich: WILEY-VCH Verlag, 2007.

[7] B. Davies. "my molecule: Carvone". *Competitions, Pedagogy*, March 30 2017, [Online]. Available: view-source: https://interactivescientific.com/2017/03/30/my-molecule-carvone/. [Accessed 31 05 2020].

[8] G. Sumithira and M. Sujatha. Drug chirality and its clinical significance evident, future for the development/separation of single enantiomer drug from racemates-the chiral switch. *International Journal of Advanced Pharmaceutical Research*, 1(1):1–19, 2013.

[9] D. Gosavi, K. Salwe, D. Vimal, and R. Gupta. Pharmacological significance of stereoisomerism. *Journal of Mahatma Gandhi Institute of Medical Sciences*, page 21, 2009.

[10] S.J. Mohan, E.C. Mohan, and M.R. Yamsani. Chirality and its importance in pharmaceutical field-an overview. *International Journal of Pharmaceutical Sciences and Nanotechnology*, 1(4):309–316, 2009.

[11] I. Agranat, H. Caner, and J. Caldwell. Putting chirality to work: the strategy of chiral switches. *Nature Reviews Drug Discovery*, 1(10):753, 2002.

[12] M.M.R. Fanood, M.HM Janssen, and I. Powis. Enantioselective femtosecond laser photoionization spectrometry of limonene using photoelectron circular dichroism. *Physical Chemistry Chemical Physics*, 17(14):8614–8617, 2015.

[13] L.D. Barron. *Molecular light scattering and optical activity*. Cambridge University Press, 2nd edition, 2004.

[14] N. Berova, K. Nakanishi, R.W. Woody, and R. Woody. *Circular dichroism: principles and applications*. New York: Wiley-VCH, second edition, 2000.

[15] U. Boesl von Grafenstein and A. Bornschlegl. Circular dichroism laser mass spectrometry: Differentiation of 3-methylcyclopentanone enantiomers. *ChemPhysChem*, 7(10):2085–2087, 2006.

[16] O. Smirnova, Y. Mairesse, and S. Patchkovskii. Opportunities for chiral discrimination using high harmonic generation in tailored laser fields. *Journal of Physics B: Atomic, Molecular and Optical Physics*, 48(23):234005, 2015.

[17] J.A. McCleverty and T.J. Meyer. *Comprehensive coordination chemistry II: from biology to nanotechnology*. Oxford: Elsevier Pergamon, second edition, 2004.

[18] A.L Nafie. *Vibrational optical activity: principles and applications*. John Wiley & Sons, first edition, July 7 2011.

[19] N. Berova, P.L. Polavarapu, K. Nakanishi, and R.W. Woody. *Comprehensive Chiroptical Spectroscopy: Instrumentation, Methodologies, and Theoretical Simulations*, volume 1. John Wiley & Sons, 2011.

[20] G.D. Fasman. *Circular dichroism and the conformational analysis of biomolecules*. New York: Springer Science and Business Media, first edition, 1996.

[21] M.H.M Janssen and I. Powis. Detecting chirality in molecules by imaging photoelectron circular dichroism. *Physical Chemistry Chemical Physics*, 16(3):856–871, 2014.

[22] I. Powis. Photoelectron circular dichroism in chiral molecules. *Advances in Chemical Physics*, 138:267–330, 2008.

[23] I. Powis. Photoelectron circular dichroism: Chiral asymmetry in the angular distribution of electrons emitted by (+)-s-carvone. *Chirality: The Pharmacological, Biological, and Chemical Consequences of Molecular Asymmetry*, 20(9):961–968, 2008.

[24] J. Miles, D. Fernandes, A. Young, CMM. Bond, SW. Crane, O. Ghafur, D. Townsend, J.Sá, and J.B Greenwood. A new technique for probing chirality via photoelectron circular dichroism. *Analytica Chimica Acta*, 984:134–139, 2017.

[25] M. Pitzer, M. Kunitski, A.S. Johnson, T. Jahnke, H. Sann, F. Sturm, L.Ph.H Schmidt, H. Schmidt-Böcking, R. Dörner, and J. Stohner. Direct determination of absolute molecular stereochemistry in gas phase by coulomb explosion imaging. *Science*, 341(6150):1096–1100, 2013.

[26] D. Patterson and M. Schnell. New studies on molecular chirality in the gas phase: enantiomer differentiation and determination of enantiomeric excess. *Physical Chemistry Chemical Physics*, 16(23):11114–11123, 2014.

[27] A. Bagga. Femtosecond laser mass spectroscopy of cyclic aromatic hydrocarbons. Master's thesis, University of Ottawa, 2017.

[28] A.F. Alharbi. High-order harmonic spectroscopy of cyclic organic molecules. PhD's thesis, University of Ottawa, 2016.

[29] R. Cireasa, AE. Boguslavskiy, B. Pons, MCH. Wong, D. Descamps, S. Petit, H. Ruf, N. Thiré, A. Ferré, and J. Suarez. Probing molecular chirality on a sub-femtosecond timescale. *Nature Physics*, 11(8):654, 2015.

[30] M. Oppermann. *Resolving Strong Field Dynamics in Cation States of CO_2 via Optimised Molecular Alignment*. Cham: Springer International Publishing: Imprint, Springer, 2014.

[31] S. Augst, D. Strickland, D.D. Meyerhofer, S.L. Chin, and J.H Eberly. Tunneling ionization of noble gases in a high-intensity laser field. *Physical review letters*, 63(20):2212, 1989.

[32] DESY. "multiphoton ionization – new opportunities at flash," deutsches elektronen-synchrotron desy a research centre of the helmholtz association, 08 12 2007, [Online]. Available: view-source:https://wof-cluster.desy.de/sites/site_photonscience/content/e58/e186104/e186825/e186879.[Accessed 31 05 2020].

[33] NB. Delone and V.P. Krainov. Energy and angular electron spectra for the tunnel ionization of atoms by strong low-frequency radiation. *JOSA B*, 8(6):1207–1211, 1991.

[34] A.G. Ciriolo, M. Negro, M. Devetta, E. Cinquanta, D. Faccialà, A. Pusala, S.De Silvestri, S. Stagira, and C. Vozzi. Optical parametric amplification techniques for the generation of high-energy few-optical-cycles ir pulses for strong field applications. *Applied Sciences*, 7(3):265, 2017.

[35] A. Ludwig, J. Maurer, BW. Mayer, CR. Phillips, L. Gallmann, and U. Keller. Breakdown of the dipole approximation in strong-field ionization. *Physical review letters*, 113(24):243001, 2014.

[36] W.C. Wiley and I.H. McLaren. Time-of-flight mass spectrometer with improved resolution. *Review of scientific instruments*, 26(12):1150–1157, 1955.

[37] W.M.A. Niessen and D. Falck. Introduction to mass spectrometry , a tutorial," in analyzing biomolecular interactions by mass spectrometry. *Weinheim, Wiley-VCH Verlag GmbH and Co. KGaA*, (2045):pp.1–45.

[38] A.D. Shiner, C. Trallero-Herrero, N. Kajumba, B.E. Schmidt, J.B. Bertrand, K.T. Kim, H-C. Bandulet, D. Comtois, J-C. Kieffer, and D.M. Rayner. High harmonic cutoff energy scaling and laser intensity measurement with a 1.8 μm laser source. *Journal of Modern Optics*, 60(17):1458–1465, 2013.

[39] S.M. Hankin, D.M. Villeneuve, P.B. Corkum and D.M. Rayner. Intense-field laser ionization rates in atoms and molecules. *Physical Review A*, 64(1):013405, June 5 2001.

[40] B. Wolter, M.G. Pullen, M. Baudisch, M. Sclafani, M. Hemmer, A. Senftleben, C.D. Schröter, J. Ullrich, R. Moshammer, and J. Biegert. Strong-field physics with mid-ir fields. *Physical Review X*, 5(2):021034, 2015.

[41] A. Emmanouilidou, T. Meltzer, and P.B Corkum. Non-dipole recollision-gated double ionization and observable effects. *Journal of Physics B: Atomic, Molecular and Optical Physics*, 50(22):225602, 2017.

[42] Model 9353 100-picosecond time digitizer hardware and software user's manual software version 2 revision e. *Advanced Measurement Technology*, ORTEC reference No. 791220 1004, 2003.